

1 **The histone modification reader ZCWPW1 links histone methylation to**
2 **PRDM9-induced double strand break repair**

3
4 Tao Huang^{1,2,3,4,5,*}, Shenli Yuan^{7,9,*}, Lei Gao^{7,9}, Mengjing Li^{1,2,3,4,5}, Xiaochen Yu^{1,2,3,4,5}, Jianhong
5 Zhang^{7,9}, Yingying Yin^{1,2,3,4,5}, Chao Liu¹⁰, Chuanxin Zhang^{1,2,3,4,5}, Gang Lu¹¹, Wei Li¹⁰, Jiang Liu^{7,8,#},
6 Zi-Jiang Chen^{1,2,3,4,5,6,#}, Hongbin Liu^{1,2,3,4,5,11,#}

7
8 ¹Center for Reproductive Medicine, Cheeloo College of Medicine, Shandong University, Jinan,
9 Shandong, China

10 ²National Research Center for Assisted Reproductive Technology and Reproductive Genetics,
11 Shandong University, Jinan, Shandong, China

12 ³Key laboratory of Reproductive Endocrinology of Ministry of Education, Shandong University, Jinan,
13 Shandong, China

14 ⁴Shandong Provincial Clinical Medicine Research Center for Reproductive Health, Shandong
15 University, Jinan, Shandong, China

16 ⁵Shandong Provincial Key Laboratory of Reproductive Medicine, Jinan, Shandong, China

17 ⁶Shanghai Key Laboratory for Assisted Reproduction and Reproductive Genetics, Shanghai, China

18 ⁷CAS Key Laboratory of Genome Sciences and Information, Beijing Institute of Genomics, Chinese
19 Academy of Sciences, Beijing, China

20 ⁸CAS Center for Excellence in Molecular Cell Science, University of Chinese Academy of Sciences,
21 Beijing, China

22 ⁹CAS Center for Excellence in Animal Evolution and Genetics, University of Chinese Academy of
23 Sciences, Beijing, China

24 ¹⁰State Key Laboratory of Stem Cell and Reproductive Biology, Institute of Zoology, Chinese
25 Academy of Sciences, Beijing, China

26 ¹¹CUHK-SDU Joint Laboratory on Reproductive Genetics, School of Biomedical Sciences, the
27 Chinese University of Hong Kong, Hong Kong, China

28

29 *These authors contributed equally to this work.

30 #Corresponding authors: liuj@big.ac.cn (J.L); chenzijiang@hotmail.com (Z-J.C);

31 hongbin_sduivf@aliyun.com (HB.L)

32

33

34 **ABSTRACT**

35 The histone modification writer PRDM9 has been shown to deposit H3K4me3 and H3K36me3 at
36 future double-strand break (DSB) sites during the very early stages of meiosis, but the reader of these
37 marks remains unclear. Here, we demonstrate that ZCWPW1 is an H3K4me3 reader that is required
38 for DSB repair and synapsis in mouse testes. We generated H3K4me3 reader-dead ZCWPW1 mutant
39 mice and found that their spermatocytes were arrested at the pachytene-like stage, which phenocopies
40 the *Zcwpw1* knock-out mice. Based on various ChIP-seq and immunofluorescence analyses using
41 several mutants, we found that ZCWPW1's occupancy on chromatin is strongly promoted by the
42 histone-modification activity of PRDM9. ZCWPW1 localizes to DMC1-labelled hotspots in a largely
43 PRDM9-dependent manner, where it facilitates completion of synapsis by mediating the DSB repair
44 process. In sum, our study demonstrates the function of ZCWPW1 that acts as part of the selection
45 system for epigenetics-based recombination hotspots in mammals.

46

47 **INTRODUCTION**

48 Meiotic recombination ensures the faithful transmission of the genome through the pairing and
49 segregation of homologous chromosomes, and it increases genetic diversity by disrupting linkage
50 relationships (Handel and Schimenti, 2010; Bolcun-Filas and Schimenti, 2012). At the molecular
51 level, meiotic recombination is initiated by the induction of programmed DSBs that are repaired by
52 homologous recombination, leading to gene conversion and cross over formation (Hunter, 2015; Gray

53 and Cohen, 2016; Zickler and Kleckner, 2015). DSB induction is a complex process, and DSB
54 locations are known to be marked at the very earliest stages of meiosis by trimethylation of histone
55 H3 on lysine 4 (H3K4me3) (de Massy, 2013; Baudat et al., 2013). In mammals, this is performed by
56 the protein PRDM9, which is expressed in the leptotene and zygotene substages (Sun et al., 2015;
57 Parvanov et al., 2017). PRDM9 is a DNA-binding zinc finger protein, with an exceptionally long and
58 genetically variable zinc finger domain that determines its binding specificity (for defining
59 recombination hotspots), while its SET domain possesses histone trimethyl transferase activity, and its
60 KRAB domain is involved in protein-protein interactions (Grey et al., 2018; Paigen and Petkov,
61 2018). In yeast, the histone reader Spp1 links H3K4me3 sites at promoters with the DSB formation
62 machinery, thus promoting DSB formation (Sommermeyer et al., 2013; Acquaviva et al., 2013). In
63 mice, although multiple studies have shown that the H3K4me3 writer PRDM9 controls the locations
64 of DSB formation (Myers et al., 2010; Parvanov et al., 2010; Baudat et al., 2010; Brick et al., 2012;
65 Powers et al., 2016; Diagouraga et al., 2018; Grey et al., 2017), much less is known about the
66 subsequent activities of any proteins that might read these epigenetic marks and thus participate in
67 advancing the meiotic recombination process (Paigen and Petkov, 2018).

68 DSB formation at sites defined by PRDM9 is catalyzed by an evolutionarily conserved
69 topoisomerase-like enzyme complex consisting of the SPO11 enzyme and its binding partner
70 TOPOVIBL (Bergerat et al., 1997; Keeney et al., 1997; Robert et al., 2016; Vrielynck et al., 2016;
71 Panizza et al., 2011). SPO11-mediated cleavage results in single-strand DNA overhangs that are
72 subsequently coated by various proteins, including DMC1 and RAD51 (Pittman et al., 1998;
73 Tarsounas et al., 1999; Dai et al., 2017). The DSBs enable homology searching and alignment to
74 occur, which in turn promote homology synapsis and DSB repair (Inagaki et al., 2010). A basic
75 feature of meiosis is that DSB-mediated interactions and repair processes occur differentially between
76 homologous nonsister chromatids, rather than between sisters, as occurs in mitotic DSB repair
77 (Keeney et al., 2014; Lange et al., 2011; Garcia et al., 2015). Some DSBs are repaired in a way that
78 generates crossovers, wherein DNA is exchanged between homologous chromosomes (Baudat and de
79 Massy, 2007). The ZMM proteins (*e.g.*, TEX11, MSH4/MSH5, and RNF212) are a group of

80 functionally related proteins known for their roles in promoting the formation of crossovers (Kneitz et
81 al., 2000; Edelmann et al., 1999; Yang et al., 2008; Lynn et al., 2007; Reynolds et al., 2013).

82 We previously reported that the zinc finger CW-type and PWWP domain containing 1
83 (ZCWPW1) protein is required for meiosis prophase I in mice, and we found that *Zcwpw1* deficiency
84 disrupted spermatogenesis in male mice but did not disrupt oogenesis in females to the same extent
85 (Li et al., 2019a). ZCWPW1 is a member of the CW-domain containing protein family (Perry and
86 Zhao, 2003; Liu et al., 2016), and its zinc finger CW (zf-CW) domain has three conserved tryptophan
87 and four conserved cysteine residues. Structural analysis has shown that human ZCWPW1 zf-CW
88 domain is a histone modification reader (He et al., 2010), while chromatin pulldown analysis has
89 confirmed that ZCWPW1 zf-CW domain recognizes H3K4me3 marks (Hoppmann et al., 2011). A
90 crystal structure of the human zf-CW domain of ZCWPW1 in complex with a peptide bearing an
91 H3K4me3 mark revealed that four amino acids– W256, E301, T302, and W303 – are primarily
92 responsible for the binding of ZCWPW1 zf-CW domain to H3K4me3 marks (He et al., 2010).
93 However, whether the H3K4me3 reading function is required for ZCWPW1's physiological role in
94 meiosis is still unknown.

95 To address the physiological role of ZCWPW1's H3K4me3 reading function, we generated an
96 H3K4me3 reader-dead *Zcwpw1* knock-in mutant mouse line (*Zcwpw1*^{KI/KI} mouse). We found that
97 spermatocytes were arrested at the pachytene-like stage, which phenocopied the defect seen in
98 *Zcwpw1* knock-out mice thus suggesting that H3K4me3 reader function of ZCWPW1 might facilitate
99 meiotic recombination by facilitating the DSB repair process. Mechanistically, a series of chromatin
100 immunoprecipitation sequencing (ChIP-seq) analyses of ZCWPW1, H3K4me3, and H3K36me3 in
101 multiple knock-out and knock-in mouse lines established that ZCWPW1 is an H3K4me3 and
102 H3K36me3 reader that exclusively binds at genomic loci bearing PRDM9-deposited histone
103 modifications. ZCWPW1 localizes to DMC1-labelled DSB hotspots where it can read H3K4me3 and
104 H3K36me3 marks. Thus, beyond demonstrating that the histone modification reader protein
105 ZCWPW1 functions in an epigenetics-based recombination hotspot selection system, this study

106 advances our understanding of the sequence of recruitment events that are required for crossover
107 formation during meiosis.

108

109 **RESULTS**

110 **The H3K4me3 reader function of ZCWPW1 is essential for meiotic recombination**

111 Previously, we developed *Zcwpw1* knockout mice in the C57BL/6 genetic background (Li et al.,
112 2019a) and found that loss of *Zcwpw1* in male mice caused a complete failure of synapsis. This failure
113 resulted in meiotic arrest at the zygotene to pachytene stage, and this was accompanied by incomplete
114 DSB repair and lack of crossover formation, thus leading to male infertility. In light of the known
115 capacity of ZCWPW1 to recognize epigenetic methylation modification marks, we designed a knock-
116 in strategy to generate a H3K4me3 reader-dead ZCWPW1 mutant mouse line (Figure 1–figure
117 supplement 1A). Specifically, this knock-in mutant of ZCWPW1 had three mutations–
118 W247I/E292R/W294P– and these mutations in mouse ZCWPW1 are equivalent to the previously
119 reported W256I, E301R, and W303P mutations in the human ZCWPW1 protein (except for T302L in
120 humans and S293 in mice, which are not conserved) (Figure 1–figure supplement 1B), and all of them
121 are known to be essential for the H3K4me3 reader function of human ZCWPW1 (He et al., 2010).

122 Western blot analysis confirmed the absence of the ZCWPW1 protein in *Zcwpw1*^{-/-} testes, while
123 the ZCWPW1^{W247I/E292R/W294P} variant protein was expressed at a level similar to that of the wild type
124 (WT) protein (Figure 1–figure supplement 2A). Consistent with the western blot data,
125 immunofluorescence staining of frozen sections from 8-week-old WT, *Zcwpw1*^{-/-}, and *Zcwpw1*^{KI/KI}
126 mouse testes revealed that the ZCWPW1 protein was undetectable in *Zcwpw1*^{-/-} spermatocytes but
127 could still be found in ZCWPW1^{W247I/E292R/W294P} mutant spermatocytes (Figure 1–figure supplement
128 2B). After confirming that the ZCWPW1^{W247I/E292R/W294P} mutant protein could be expressed normally in
129 *Zcwpw1*^{KI/KI} mice, we prepared testis sections from 8-week-old WT, *Zcwpw1*^{-/-}, and the new
130 *Zcwpw1*^{KI/KI} mouse line. Hematoxylin staining showed that spermatogenesis was disrupted in both the
131 *Zcwpw1*^{-/-} and *Zcwpw1*^{KI/KI} mice. Compared with the WT mice, the seminiferous tubules of the
132 *Zcwpw1*^{-/-} and *Zcwpw1*^{KI/KI} mice lacked post-meiotic cell types, contained apoptotic cells, or were

133 nearly empty. Furthermore, the WT epididymides were full of sperm, but there were no obvious sperm
134 detected in either the *Zcwpw1*^{-/-} or *Zcwpw1*^{K1/K1} samples, suggesting meiotic arrest in these mice
135 (Figure 1A).

136 We then analyzed chromosome spreads of spermatocytes from the testes of adult mice by
137 immunostaining for the synaptonemal complex (SC) markers SYCP1 and SYCP3 (Figure 1B).
138 Immunostaining of SYCP1 and SYCP3 showed no differences among any of the genotypes with
139 regard to leptotene-to-zygotene progression, which appeared normal in all mice. We quantified the
140 synapsed chromosome pairs in the nuclei of WT, *Zcwpw1*^{-/-}, and *Zcwpw1*^{K1/K1} testes from 8-week-old
141 mice. We observed 169 spermatocytes in WT testes, and 153 spermatocytes (90.5%) had all
142 chromosome pairs fully synapsed, with only 16 spermatocytes (9.5%) exhibiting synapsis between 4
143 and 18 pairs of chromosomes. In contrast, among 164 spermatocytes in *Zcwpw1*^{-/-} testes and 158
144 spermatocytes in *Zcwpw1*^{K1/K1} testes none had complete synapsis, and we only detected around of 8
145 synapsed chromosome pairs in *Zcwpw1*^{-/-} and *Zcwpw1*^{K1/K1} spermatocytes (Figure 1–figure
146 supplement 2C) (Li et al., 2019a). Thus, spermatocytes lacking the H3K4me3-reader activity of the
147 ZCWPW1 protein have severely disrupted synapsis.

148 Having established that ZCWPW1 facilitates the completion of synapsis during meiosis prophase
149 I in male mice, we observed that the ZCWPW1^{W247I/E292R/W294P} mutant mice exhibited the same
150 synapsis defect as *Zcwpw1* knockout mice, suggesting that these residues are essential for the
151 recombination-related functions of ZCWPW1. We then performed immunofluorescence staining of
152 chromosome spreads to evaluate the recruitment of DMC1 and RAD51 to single-stranded overhang
153 sequences (hotspots) in WT and *Zcwpw1*^{K1/K1} mice (Figure 1C and E). There were no differences in the
154 numbers of DMC1 or RAD51 foci in the leptotene or zygotene stages of the two genotypes. However,
155 analysis of WT pachytene and *Zcwpw1*^{K1/K1} pachytene-like spermatocytes revealed an obvious
156 discrepancy. Decreased numbers of DMC1 and RAD51 foci were seen in the pachytene WT
157 spermatocytes, indicating successful repair of DSBs, but the *Zcwpw1*^{K1/K1} pachytene-like
158 spermatocytes retained a large number of DMC1 and RAD51 foci (Figure 1D and F). These results
159 suggest that the repair of DSBs is disrupted in the absence of a functional ZCWPW1 H3K4me3 reader
160 protein and that ZCWPW1 might facilitate meiotic DSB repair downstream of strand invasion.

161 Seeking to further assess the functional contributions of ZCWPW1 in meiotic recombination, we
162 analyzed chromosome spreads of spermatocytes from the testes of adult WT and *Zcwpw1^{KI/KI}* mice by
163 immunostaining for the recombination factors MSH4 and RNF212 and the Holliday junction
164 dissolution marker MLH1 (Figure 1–figure supplement 3A and C and E). Staining for MSH4 and
165 RNF212 showed that the recombination machinery could assemble normally in both WT and
166 *Zcwpw1^{KI/KI}* spermatocytes at the zygotene stage. However, these MSH4 and RNF212 signals
167 decreased as expected in WT pachytene spermatocytes, but persisted on the pachytene-like
168 *Zcwpw1^{KI/KI}* chromosomes (Figure 1–figure supplement 3B and D). Additionally, the MLH1 staining
169 patterns indicated that Holliday junction dissolution proceeded normally in mid- to late-pachytene
170 WT spermatocytes but indicated that the recombination process was arrested in the pachytene-like
171 spermatocytes lacking ZCWPW1 H3K4me3-reader function, which failed to progress to the
172 pachytene stage and for which no crossover occurred, thus resulting in the absence of MLH1 foci
173 (Figure 1–figure supplement 3E). These results suggest that DSB repair is defective downstream of
174 the formation of recombination intermediates in the *Zcwpw1^{KI/KI}* mice.

175 To determine the specific process that can mechanistically account for the observed failure to
176 complete meiotic recombination, we stained the spreads of spermatocytes from the testes of adult WT,
177 *Zcwpw1^{-/-}*, and *Zcwpw1^{KI/KI}* mice for the DSB marker γ H2AX. We found that DSBs could form
178 normally in all of the genotypes (Figure 2A), but there were obvious differences between pachytene
179 WT spermatocytes and pachytene-like *Zcwpw1^{-/-}* and *Zcwpw1^{KI/KI}* spermatocytes. The WT pachytene
180 spermatocytes exhibited no obvious signal for DSB sites on autosomes, but retained such signals on
181 the sex chromosomes, while both autosomes and sex chromosomes in *Zcwpw1^{-/-}* and *Zcwpw1^{KI/KI}*
182 pachytene-like spermatocytes retained obvious γ H2AX signals. Moreover, XY bodies formed in the
183 WT pachytene spermatocytes but were not observed in the pachytene-like *Zcwpw1^{-/-}* and *Zcwpw1^{KI/KI}*
184 spermatocytes. We next stained against the DSB-repair machinery component p-ATM and found that
185 DSB repair was apparently not finished in the pachytene-like *Zcwpw1^{-/-}* or *Zcwpw1^{KI/KI}*
186 spermatocytes (Figure 2B). Through single-stranded DNA sequencing (SSDS) by ChIP-seq against
187 DMC1, Wells *et al.* found that DSBs occur in the same hotspot regions in *Zcwpw1^{-/-}* male mice

188 (Wells et al., 2019). Similarly, using quantitative END-seq, Mahgoub *et al.* also confirmed that
189 DSBs in both WT and *Zcwpw1*^{-/-} mice completely overlapped with each other and with previously
190 identified hotspots (Mahgoub et al., 2019). These data indicate that these key ZCWPW1 residues are
191 dispensable for the induction and location of DSBs but are required for proper interhomolog
192 interactions including synapsis and the repair of DSBs that occur in the later steps of homologous
193 recombination.

194

195 **ZCWPW1 is an H3K4me3/H3K36me3 reader**

196 Having thus established that ZCWPW1 promotes the completion of synapsis and that it functions
197 in meiotic recombination by facilitating DSB repair, we next investigated the mechanism by which
198 ZCWPW1 recognizes histone modification marks involved in male meiosis prophase I. To this end,
199 we conducted ChIP-seq using antibodies against the ZCWPW1 protein and against H3K4me3 marks.
200 The ZCWPW1 ChIP-seq data for C57BL/6 mice revealed a total of 14,688 ZCWPW1 peaks, with 499
201 peaks localized within 2,000 bp upstream of a transcription start site (TSS), 2,416 peaks localized in
202 exons, 6,142 peaks localized in introns, and 5,873 peaks localized within intergenic regions (Figure
203 3-figure supplement 1A).

204 Among all ZCWPW1 binding sites detected in mouse testes, 11.5% of the ZCWPW1 binding sites
205 (peaks) overlapped with promoters, while 6.1% of ZCWPW1 binding sites overlapped with CpG
206 islands (Figure 3-figure supplement 1B). Compared with the random binding sites, ZCWPW1
207 binding sites were not significantly enriched in the transposable element regions (Figure 3-figure
208 supplement 1C D). In HEK293T cells, Wells *et al.* found that a large proportion of the weakly-binding
209 ZCWPW1 sites overlapped with Alu repeats. Notably, the weakest ZCWPW1 peaks overlapped most
210 frequently with Alus repeats, while the strongest peaks were depleted of Alus repeats relative to
211 random overlap. They also found that ZCWPW1 appears to have a greater affinity for methylated
212 CpG pairs but retains some affinity even for non-methylated regions (Wells et al., 2019). Because we
213 found that 1,766 of the ZCWPW1 binding sites overlapped with promoters, we sought to examine the
214 transcriptome in *Zcwpw1*^{-/-} testes by RNA-seq to investigate whether ZCWPW1 affected the

215 expression of those genes whose promoters overlapped with ZCWPW1 binding sites. Analysis of
216 RNA-seq data of postnatal day 14 (PD14) WT and *Zcwpw1*^{-/-} mice identified 567 differentially
217 expressed genes (DEGs), including 464 downregulated and 103 upregulated DEGs in *Zcwpw1*^{-/-}
218 testes compared with WT testes (Figure 3–figure supplement 2A). Gene ontology analysis showed
219 that the down-regulated genes were enriched in axoneme assembly, male gamete generation and
220 flagellated sperm motility (Figure 3–figure supplement 2B). However, most of the DEGs were not the
221 genes whose promoters overlapped with ZCWPW1 binding sites (Figure 3–figure supplement 2C).
222 These data strongly suggest that ZCWPW1 might not affect the transcription level of genes even
223 though it can bind to their promoter regions.

224 The H3K4me3 ChIP-seq data in C57BL/6 mice revealed a total of 55,801 H3K4me3 peaks,
225 consistent with a previous report of 55,497 H3K4me3 peaks in whole testes (Smagulova et al., 2011).
226 Lam *et al.* described a method for isolating pure sub-populations of meiotic substage nuclei, and they
227 detected a total of 75,771 H3K4me3 peaks in isolated SCP3⁺H1T⁻ spermatocytes (Lam et al., 2019).
228 In our work, we obtained a weaker average H3K4me3 signal in ZCWPW1 peaks in whole testes than
229 that reported by Lam *et al.* in isolated, stage-specific spermatocyte nuclei (Figure 3C). The ChIP-seq
230 data from sorted meiotic cells thus allowed the elimination of H3K4me3 peaks originating from cells
231 that did not express ZCWPW1. In light of the known capacity of ZCWPW1 to recognize epigenetic
232 methylation modification marks, we compared the ZCWPW1 peaks with these two sets of H3K4me3
233 peaks, and we found that 97.8% (14,369 of 14,688 peaks) of the ZCWPW1 peaks overlapped with the
234 H3K4me3 peaks reported by Lam *et al.*, while 39.4% (5,792 of 14,688 peaks) of the ZCWPW1 peaks
235 overlapped with the H3K4me3 peaks in our data (Figure 3A and B), therefore supporting the
236 hypothesis that this specific overlap with H3K4me3 peaks serves as a means for ZCWPW1
237 recognition of histone modification marks.

238 To determine whether H3K4me3 marks are necessary for ZCWPW1 recruitment to chromatin *in*
239 *vivo*, we conducted an additional ZCWPW1 ChIP-seq analysis of testes samples from PD14 WT,
240 *Zcwpw1*^{-/-}, and *Zcwpw1*^{K1/K1} mice. The analysis indicated that no ZCWPW1 peaks were detected in
241 the *Zcwpw1*^{-/-} or *Zcwpw1*^{K1/K1} mice (Figure 3A and D). These *in vivo* results, viewed alongside the
242 previous reports of ZCWPW1 function in the meiotic process demonstrating that these specific

243 mutations in the ZCWPW1 zf-CW domain affect the protein's ability to read histone modifications
244 (including H3K4me3), together indicate that the ZCWPW1^{W247I/E292R/W294P} mutant is an H3K4me3
245 reader-dead variant of ZCWPW1. Furthermore, these results suggest that the H3K4me3 reader
246 function of this protein is essential for its ability to bind to chromatin and to function in meiosis
247 prophase I in male mice.

248 ZCWPW1 also has a PWWP domain which was found in multiple other proteins to specifically
249 bind to histone H3 containing an H3K36me3 mark (Qin et al., 2014), so we next sought to better
250 understand the overlap between ZCWPW1 peaks and H3K36me3 peaks in our ChIP-seq dataset. We
251 found that 90.1% of the ZCWPW1 peaks overlapped with the H3K36me3 peaks reported by Lam *et*
252 *al.* in isolated stage-specific spermatocyte nuclei, while 24.8% of the ZCWPW1 peaks overlapped
253 with the H3K36me3 peaks identified by Grey *et al.* in whole testes (Figure 3–figure supplement 3A).
254 As with our data from whole testes, the average H3K36me3 signal of ZCWPW1 peaks obtained by
255 Grey *et al.* was considerably weaker than that from isolated stage-specific spermatocyte nuclei
256 obtained by Lam *et al.* (Figure 3–figure supplement 3B).

257 In analyzing the correlation between ZCWPW1 binding sites and these two histone modification
258 marks, we found that 88.8% of the ZCWPW1 peaks overlapped with regions containing both
259 H3K4me3 and H3K36me3 marks, while only 9.1% and 1.3% of ZCWPW1 peaks overlapped with
260 H3K4me3 and H3K36me3 peaks individually (Figure 3E). Furthermore, the ZCWPW1 peak intensity
261 was significantly higher for the dual overlapping regions than for regions containing either H3K4me3
262 or H3K36me3 alone (Figure 3–figure supplement 3C). We also found that ZCWPW1 bound
263 H3K4me3 regions had higher H3K36me3 levels than H3K4me3 regions were not bound by
264 ZCWPW1 (Figure 3–figure supplement 3D). We conducted immunofluorescence analysis of
265 chromosome spreads of spermatocytes from adult mice using rat anti-ZCWPW1 and rabbit anti-
266 H3K4me3/H3K36me3 antibodies and found, consistent with the ChIP-seq data, that both H3K4me3
267 and H3K36me3 were highly correlated with the ZCWPW1 expression pattern in the leptotene and
268 zygotene stages (Figure 3–figure supplement 4A-B). Moreover, Mahgoub *et al.* (2019) confirmed that
269 recombinant ZCWPW1 (1–440aa) binds with the highest affinity to H3K4me3/K36me3 peptides *in*

270 *vitro*. Taken together, these results demonstrate that ZCWPW1 preferentially binds to sites with both
271 H3K4me3 and H3K36me3 marks.

272

273 **ZCWPW1 binding is strongly promoted by the histone modification activity of PRDM9**

274 To identify the factors responsible for ZCWPW1 recruitment to chromatin *in vivo*, we searched for
275 enriched motifs within the ZCWPW1 binding sites in our ChIP-seq data (Figure 4–figure supplement
276 1A). This analysis identified a *de novo* motif that is highly correlated with a known PRDM9 binding
277 motif in mice (Figure 4-figure supplement 1B) (Segurel, 2013; Billings et al., 2013; Walker et al.,
278 2015), and this suggested that ZCWPW1 binding to chromatin might occur in a PRDM9-dependent
279 manner. To pursue this possibility, we compared our ZCWPW1 ChIP-seq data with previously
280 published ChIP-seq data generated using an anti-PRDM9 antibody and with data from an affinity-seq
281 analysis of genome-wide PRDM9 binding sites (Grey et al., 2017; Walker et al., 2015). At the
282 genome-wide level, 13% of the ZCWPW1 peaks obtained in our study overlapped with Grey *et al.*'s
283 PRDM9 peaks, while 74% of the ZCWPW1 peaks overlapped with Walker *et al.*'s PRDM9 peaks.
284 Conversely, we found that 1,934 of 2,601 PRDM9 peaks (74%) from Grey *et al.* and 10,975 of 36,898
285 PRDM9 peaks (29.7%) from Walker *et al.* overlapped with our ZCWPW1 peaks (Figure 4A and B).
286 The high overlap between ZCWPW1 and PRDM9 peaks further suggested that ZCWPW1 occupancy
287 occurs in a PRDM9-dependent manner.

288 To further explore this finding of high overlap between ZCWPW1 and PRDM9 peaks in our
289 ChIP-seq data, and in light of the well-known overlap of PRDM9 peaks with H3K4me3 and
290 H3K36me3 marks (Grey et al., 2017; Diagouraga et al., 2018; Powers et al., 2016), we compared the
291 ZCWPW1/PRDM9 overlap with the ZCWPW1/histone mark overlap. We found that the majority of
292 ZCWPW1 peaks overlapped with PRDM9 binding sites containing both H3K4me3 and H3K36me3
293 marks (Figure 4A and C, Figure 4–figure supplement 1C and F). Our further analysis of H3K4me3
294 peak intensity in whole testes showed that among the PRDM9-occupied regions from Grey *et al.*, the
295 intensity of H3K4me3 peaks overlapping with ZCWPW1 was significantly weaker than that of
296 ZCWPW1-non-overlapping regions (Figure 4–figure supplement 1D left panel), which was consistent
297 with previous reports (Smagulova et al., 2011). In contrast, the H3K4me3 and H3K36me3 peak

298 intensities of isolated stage-specific spermatocyte nuclei (Lam *et al.*) showed that among the PRDM9-
299 occupied regions from Grey *et al.* and Walker *et al.*, the intensities of H3K4me3 and H3K36me3
300 peaks overlapping with ZCWPW1 were significantly greater than the intensities of ZCWPW1-non-
301 overlapping regions (Figure 4–figure supplement 1D and E). Allowing for differences in the binding
302 performance of different antibodies in different ChIP-seq analyses, the fact that some but certainly not
303 all of the ZCWPW1 peaks overlapped with PRDM9 peaks suggests that it is the H3K4me3 and
304 perhaps H3K36me3 epigenetic marks deposited by PRDM9, rather than the PRDM9 protein *per se*,
305 that can explain the observed overlap of the ZCWPW1 and PRDM9 peaks.

306 To determine whether the activity of PRDM9 is necessary for ZCWPW1 recruitment to chromatin
307 *in vivo*, we conducted an additional ZCWPW1 and H3K4me3 ChIP-seq analysis of testes samples
308 from PD14 WT and *Prdm9*^{-/-} mice (Figure 1–figure supplement 1C). Consistent with a previous
309 report (Brick *et al.*, 2012), the majority of PRDM9-dependent H3K4me3 peaks disappeared in
310 *Prdm9*^{-/-} mice (Figure 4D and E, Figure 4–figure supplement 2A-C). In our ChIP-seq data, we found
311 that the H3K4me3 peaks overlapped with PRDM9 binding sites (Grey *et al.*, 2017); however, with the
312 exception of a lack of ZCWPW1 binding sites, no obvious difference could be found between WT and
313 *Prdm9*^{-/-} testes (Figure 4E right panel, Figure 4–figure supplement 2A). These results led us to
314 speculate that in addition to PRDM9 functioning as an indispensable methyltransferase in meiosis, it
315 might also act as a reader for recognizing H3K4me3 modifications. Intriguingly, there were very few
316 ZCWPW1 peaks for the *Prdm9*^{-/-} mutant testes samples (only 781 peaks, vs. 14,668 ZCWPW1 peaks
317 observed in the ChIP-seq analysis of the WT C57BL/6 mice), and this suggested that ZCWPW1
318 binding is strongly promoted by the specific activity of PRDM9 (Figure 4D and E, Figure 4–figure
319 supplement 2A-C).

320 Having established that ZCWPW1 binding to chromatin is strongly promoted by the histone
321 modification activity of PRDM9, we next examined changes in ZCWPW1 binding sites between WT
322 and *Prdm9*^{-/-} mutant testes. We found that although 94.7% of the ZCWPW1 peaks were apparently
323 lost in *Prdm9*^{-/-} mutant testes, 781 ZCWPW1 peaks were maintained and were accompanied by 652
324 newly generated ZCWPW1 peaks in *Prdm9*^{-/-} mice (Figure 4–figure supplement 3A). Furthermore,
325 examination of peak intensities showed that the new ZCWPW1 peaks were significantly weaker than

326 those of both the maintained and the lost ZCWPW1 peaks in *Prdm9*^{-/-} mice (Figure 4–figure
327 supplement 3B). The majority of these gained (67.8%) and maintained (83.2%) ZCWPW1 peaks
328 overlapped with promoter regions, while only 7.4% of the lost ZCWPW1 peaks overlapped with
329 promoter regions in *Prdm9*^{-/-} mice (Figure 4–figure supplement 3C). Further analysis showed that
330 nearly 80% of the lost ZCWPW1 peaks overlapped with PRDM9 binding sites, while the majority of
331 the maintained and gained ZCWPW1 peaks did not overlap with PRDM9 peaks (Figure 4–figure
332 supplement 3D). Surprisingly, a motif analysis showed that 3,028 ZCWPW1 peaks, *i.e.*, those that
333 were lost and did not overlap with PRDM9 binding sites, were significantly enriched at PRDM9
334 binding sites (Figure 4–figure supplement 3E), suggesting that ZCWPW1 binding to these sites is
335 highly PRDM9 dependent.

336

337 **ZCWPW1 localizes to DMC1-labelled DSB hotspots in a PRDM9-dependent manner**

338 A previous study developed a novel method—SSDS analysis using an antibody against DMC1 in
339 mouse testes—that specifically detects protein-bound single-stranded DNA at DSB ends (Khil et al.,
340 2012; Grey et al., 2017). SSDS provides insights into the shape and evolution of the mammalian DSB
341 landscape (Davies et al., 2016). Lange *et al.* sequenced mouse SPO11 oligos and provided nucleotide-
342 resolution DSB maps with low background and high dynamic range and found that SPO11 oligo
343 counts correlated well with SSDS coverage (Lange et al., 2016). A previously study found that 94% of
344 DMC1-labeled hotspots overlapped with H3K4me3 in the testis, and this can be considered a global
345 feature of DSB sites in multicellular organisms (Smagulova et al., 2011). Because we found that
346 ZCWPW1 recognized dual histone modifications via PRDM9, we compared the distribution of the
347 ZCWPW1 peaks with the DMC1 peaks and SPO11 oligos in the publicly available datasets (Grey et
348 al., 2017; Lange et al., 2016). For the WT mice, 11,124 of the 14,688 total ZCWPW1 peaks
349 overlapped with DMC1-defined DSB hotspots, while 10,340 of ZCWPW1 peaks overlapped with
350 SPO11 oligo-defined DSB hotspots (Figure 5–figure supplement 1A). The heatmap and profile plot
351 showed high correlation between the ZCWPW1 signals and all of the DMC1 peaks (Figure 5–figure
352 supplement 1B). Specifically, the greater the ZCWPW1 peak intensity, the better the overlap between

353 the ZCWPW1 peaks and the DMC1 peaks (Figure 5–figure supplement 1C). These results strongly
354 suggest that ZCWPW1 localizes to DMC1-labelled DSB hotspots.

355 Further analysis showed that 65.1% of the DMC1 peaks overlapped with both ZCWPW1 binding
356 sites and merged PRDM9 peaks (Figure 5–figure supplement 1D). Our ZCWPW1 and H3K4me3
357 ChIP-seq data in WT and *Prdm9*^{-/-} mice indicated an apparent lack of ZCWPW1 peaks and H3K4me3
358 signals at DMC1-labelled DSB hotspots (Figure 5A and B). Among all of the ZCWPW1 peaks lost in
359 *Prdm9*^{-/-} mice, group II showed high overlap with both PRDM9 peaks and DMC1-labelled DSB
360 hotspots, while group I showed overlap with DMC1-labelled DSB hotspots without PRDM9 binding
361 sites (Figure 5B). However, motif analysis predicted that these group I ZCWPW1 peaks could be
362 significantly enriched at PRDM9 binding sites (Figure 4–figure supplement 3E) accompanied by
363 H3K4me3 lost at these ZCWPW1 binding sites (Figure 5B). These data reinforce the idea that
364 occupancy of ZCWPW1 at DMC1-labelled DSB hotspots is largely dependent on PRDM9-mediated
365 histone modifications.

366 However, it bears mentioning that we also detected 781 ZCWPW1 peaks in WT testes that did not
367 obviously overlap with DSB hotspots and we detected 652 ZCWPW1 peaks that did not obviously
368 overlap with DSB hotspots in *Prdm9*^{-/-} mice (Figure 5B, Figure 4–figure supplement 3A). We
369 analyzed these 781 ZCWPW1 binding sites in detail and we found that 83.2% of these maintained
370 peaks occurred within 5,000 bp of a TSS, a substantially larger proportion than for the average
371 position among all lost ZCWPW1 peaks (Figure 5–figure supplement 1E). We also found that the
372 distribution pattern of H3K4me3 and H3K36me3 peaks, which overlapped with those 1,433
373 ZCWPW1 peaks, was significantly different compared to the distribution pattern of H3K4me3 and
374 H3K36me3 peaks that overlapped with DMC1-labelled DSB hotspots (Figure 5B). Thus, although it
375 is clear that the majority of the ZCWPW1 peaks resulted from PRDM9 activity, it is possible that
376 ZCWPW1 might have an additional transcription regulation function that is not obviously related to
377 the PRDM9-mediated hotspot selection system.

378

379 **DISCUSSION**

380 Our data support a working model wherein PRDM9 binds to specific DNA motifs in the genome and
381 writes histone modifications (H3K4me3 and H3K36me3) via the methyltransferase activity of its
382 PR/SET domain (Powers et al., 2016; Diagouraga et al., 2018). This leads to the recruitment of
383 proteins required for the formation of DSBs in the vicinity of its binding site (e.g., SPO11, etc.)
384 (Panizza et al., 2011; Stanzione et al., 2016; Tesse et al., 2017; Kumar et al., 2018). After these
385 PRDM9-catalyzed epigenetic modifications are deposited, ZCWPW1 can specifically read these
386 H3K4me3 and H3K36me3 marks in the vicinity of DSB sites, where it functions to promote DSB
387 repair. This DSB-repair-promoting function greatly increases the overall completion rates of synapsis,
388 crossover formation, and ultimately meiotic progression.

389 The identification of recombination hotspots was first made in genetically-tractable experimental
390 organisms such as bacteriophages and fungi, but it is now apparent that such hotspots are ubiquitous
391 and active in all organisms (Wahls, 1998). Higher-order chromosome architecture, which can be
392 described using the terminology of the “tethered-loop/axis complex” model, contributes to DSB
393 hotspot localization (Blat et al., 2002), and different strategies and mechanisms for the spatial
394 regulation of DSB formation have evolved in different species, although these have many common
395 features (de Massy, 2013; Baudat et al., 2013). In considering the evolution of hotspot selection
396 systems, we are interested in whether other meiotic factors might have evolved in vertebrates to link
397 PRDM9 to the meiotic recombination machinery and/or the synaptonemal complex, which would
398 permit direct interactions with the histone marks deposited by PRDM9.

399 In *Saccharomyces cerevisiae*, Spp1—whose PHD finger domain is known to read H3K4me3
400 marks—promotes meiotic DSB formation by interacting with the axis-bound Spo11 accessory protein
401 Mer2 (Sommermeyer et al., 2013; Acquaviva et al., 2013). Our study in mammals supports that one or
402 more other as-yet unknown proteins might function in a similar role during DSB formation. It is
403 noteworthy that there is structural similarity between the zf-CW domain and the PHD finger of Spp1
404 that helps recognize histone H3 tails (Adams-Cioaba and Min, 2009). Moreover, structural analysis
405 has indicated that the zf-CW domain of human ZCWPW1 is a histone modification reader (He et al.,
406 2010), and chromatin pulldown analysis has confirmed that this domain recognizes H3K4me3 marks
407 (Hoppmann et al., 2011). In the present study, we showed that ZCWPW1 can specifically read

408 H3K4me3 and H3K36me3 marks in the vicinity of DSB sites. However, somewhat surprisingly, our
409 subsequent experiments indicated that deficiency of ZCWPW1 did not affect the recruitment of
410 recombination-related factors like DMC1, MSH4, or RNF212, thereby implying that there might be
411 other unknown proteins that function to link PRDM9 to meiotic recombination machinery.

412 The zf-CW domain of ZCWPW1 has previously been shown to bind to H3K4me3 peptides (He et
413 al., 2010), and the PWWP domain, another type of “reader” module, has been shown to recognize
414 H3K36me3 in both peptide and nucleosome contexts (Eidahl et al., 2013; Rondelet et al., 2016;
415 Vezzoli et al., 2010). Consistent with a recently deposited pre-print at bioRxiv showing that
416 ZCWPW1 can bind to histone H3 peptides with double H3K4me3 and H3K36me3 marks with high
417 affinity at a 1:1 ratio *in vitro* (Mahgoub et al., 2019), we also found that ZCWPW1 localized to
418 H3K4me3 and H3K36me3 enrichment regions in ChIP-seq analysis. Notably, most of the ZCWPW1
419 peaks overlapping H3K4me3 peaks disappeared in *Prdm9* knockout mice. One functional implication
420 of our study is that it is PRDM9's histone modification activity, rather than the chromatin residence of
421 the PRDM9 protein *per se*, that might account for the functional interactions of the apparently co-
422 involved ZCWPW1 and PRDM9 proteins.

423 Our H3K4me3 reader-dead mutant mice showed that, upon loss of the binding affinity of the
424 ZCWPW1 zf-CW domain for H3K4me3 marks, the ZCWPW1 protein completely lost its ability to
425 bind chromatin, and spermatocytes in mice expressing this knock-in H3K4me3 reader-dead mutant
426 ZCWPW1 exhibited a nearly complete failure of meiosis prophase I. We also hypothesize that this
427 protein is unable to bind unmodified histones, that is, the mutant protein might be a histone binding-
428 dead variant in addition to being a reader-dead variant. However, it remains unclear whether the
429 ZCWPW1 PWWP domain, which likely functions in reading H3K36me3 marks, and/or other regions
430 of the ZCWPW1 protein confer similarly important functions. Indeed, in future work we plan to
431 pursue the selective disruption of the function of particular ZCWPW1 domains in our attempts to
432 elucidate this protein's functions in male meiosis I.

433 While we clearly show that ZCWPW1 greatly facilitates PRDM9-dependent DSB repair, we do
434 not yet have strong evidence for the precise nature of its functional role. One possibility is that
435 ZCWPW1, upon binding to PRDM9-dependent histone modification hotspots, might serve as a DSB

436 mark, which can perhaps subsequently recruit other factors involved in DSB repair. Recent studies
437 have reported that PRDM9 binds on both the cut and uncut template chromosomes to promote meiotic
438 recombination (Hinch et al., 2019; Li et al., 2019b). It is also possible that ZCWPW1 might directly
439 interact with the SC machinery by using its SCP1-like domain to tether PRDM9-bound loops to the
440 SC in order to promote homologous DSB repair.

441 In summary, our study identifies ZCWPW1 as an H3K4me3 and H3K36me3 reader that promotes
442 the repair of DNA DSBs during meiotic recombination, thus not supporting previous hypotheses that
443 this protein directs the location or the formation of DSBs (Mahgoub et al., 2019; Wells et al., 2019).
444 In future studies, we plan to focus on additional proteins (*e.g.*, ZCWPW2, MORC3/4, etc.) that have
445 similar functional domains as ZCWPW1 (Liu et al., 2016), with the aim of identifying any unknown
446 biomolecules that might act to link PRDM9 to the DSB machinery specifically or to meiotic
447 recombination more generally.

448

449 MATERIALS AND METHODS

450

451 Mice

452 The *Zcwpw1* gene (NCBI Reference Sequence: NM_001005426.2) is located on mouse chromosome
453 5 and comprises 17 exons, with its ATG start codon in exon 2 and a TAG stop codon in exon 17. The
454 *Zcwpw1* knockout mice were generated in our previous study (Li et al., 2019a). The *Zcwpw1* knock-in
455 H3K4me3-reader-dead mutant mice were generated by mutating three sites. The W247I (TGG to
456 ATT) point mutation was introduced into exon 8 in the 5' homology arm, and the E292R (GAG to
457 CGG) and W294P (TGG to CCG) point mutations were introduced into exon 9 in the 3' homology
458 arm. The W247I, E292R, and W294P mutations created in the mouse *Zcwpw1* gene are positionally
459 equivalent to the W256I, E301R, and W303P mutations previously reported in the human *ZCWPW1*
460 gene. To engineer the targeting vector, homology arms were generated by PCR using BAC clones
461 RP24-387B18 and RP24-344E7 from the C57BL/6 library as templates. In the targeting vector, the
462 Neo cassette was flanked by SDA (self-deletion anchor) sites. DTA was used for negative selection.
463 C57BL/6 ES cells were used for gene targeting, and genotyping was performed by PCR amplification

464 of genomic DNA extracted from mouse tails. PCR primers for the *Zcwpw1* Neo deletion were
465 Forward: 5'-CAC TGA GTT AAT CCC ACC TAC GTC-3' and Reverse: 5'CTC TCC CAA ACC ATC
466 TCA AAC ATT-3', with targeted point mutants yielding a 318 bp fragment and WT mice yielding a
467 174 bp fragment (Cyagen Biosciences Inc, Guangzhou, China).

468 The mouse *Prdm9* gene (GenBank accession number: NM_144809.3) is located on mouse
469 chromosome 17. Ten exons have been identified, with the ATG start codon in exon 1 and the TAA
470 stop codon in exon 10. The *Prdm9* knockout mice in the C57BL/6 genetic background were generated
471 by deleting the genomic DNA fragment covering exon 1 to exon 9 using the CRISPR/Cas9-mediated
472 genome editing system (Cyagen Biosciences Inc, Guangzhou, China). The founders were genotyped
473 by PCR followed by DNA sequencing analysis. Genotyping was performed by PCR amplification of
474 genomic DNA extracted from mouse tails. PCR primers for the *Prdm9* mutant allele were Forward:
475 5'-GCT TAG GTA GCA GAA TTG AAG GGA AAG TC-3' and Reverse: 5'- GTT TGT GTC TTT
476 CTA ACT CAA ACT TCT GCA-3', yielding a 580 bp fragment. PCR primers for the *Prdm9* WT
477 allele were Forward: 5'- GCT TAG GTA GCA GAA TTG AAG GGA AAG TC-3' and Reverse: 5'-
478 TCG TGG CGT AAT AAT AGA GTG CCT TG-3', yielding a 401 bp fragment.

479 All mice were housed under controlled environmental conditions with free access to water and
480 food, and illumination was on between 6 a.m. and 6 p.m. All experimental protocols were approved
481 by the Animal Ethics Committee of the School of Medicine of Shandong University.

482

483 **Production of the rat ZCWPW1 antibody**

484 Antibodies to mouse ZCWPW1 were produced by Dia-an Biological Technology Incorporation
485 (Wuhan, China). Briefly, a complementary DNA (cDNA) fragment encoding amino acids 448 to 622
486 of mouse

487 *Zcwpw1* was inserted into the p-ET-32a + vector (EMD Millipore) and transfected into BL21-
488 CodonPlus (DE3) *Escherichia coli* cells. The cells were cultured at 37°C overnight and induced by
489 addition of 0.2 mM isopropyl-1-thio- β -d-galactoside (Sigma-Aldrich) for 4 hours at 28°C. Cells
490 were

491 harvested by centrifugation and disrupted by sonication, and the soluble homogenates were purified
492 by Ni-nitrilotriacetic acid (NI-NTA) Agarose (Qiagen) according to the manufacturer's instructions.
493 The protein was dialyzed in phosphate-buffered saline (PBS) and used to immunize rats, and the
494 antiserum was affinity-purified on antigen-coupled CNBr-activated agarose (GE Healthcare).

495

496 **Tissue collection and histological analysis**

497 Testes from at least three mice for each genotype were dissected immediately after euthanasia, fixed
498 in 4% (mass/vol) paraformaldehyde (Solarbio) for up to 24 h, stored in 70% ethanol, and embedded in
499 paraffin after dehydration, and 5 μ m sections were prepared and mounted on glass slides. After
500 deparaffinization, slides were stained with hematoxylin for histological analysis using an
501 epifluorescence microscope (BX52, Olympus), and images were processed using Photoshop (Adobe).

502

503 **Chromosome spread immunofluorescence analysis**

504 Spermatocyte spreads were prepared as previously described (Peters et al., 1997). Primary antibodies
505 used for immunofluorescence were as follows: rabbit anti-ZCWPW1 (1:1,000 dilution; Dia-an
506 Biological Technology Incorporation (Li et al., 2019a)), rat anti-ZCWPW1 (1:200 dilution; Dia-an
507 Biological Technology Incorporation), mouse anti-SCP3 (1:500 dilution; Abcam #ab97672), rabbit
508 anti-SCP1 (1:2,000 dilution; Abcam # ab15090), rabbit anti-RAD51 (1:200 dilution; Thermo Fisher
509 Scientific #PA5-27195), rabbit anti-DMC1 (1:100 dilution; Santa Cruz Biotechnology #sc-22768),
510 mouse anti- γ H2AX (1:300 dilution; Millipore #05-636), mouse anti-pATM (1:500 dilution; Sigma-
511 Aldrich #05-740), rabbit anti-MSH4 (1:500 dilution; Abcam #ab58666), rabbit anti-RNF212 (1:500
512 dilution; a gift from Mengcheng Luo, Wuhan University), mouse anti-MLH1 (1:50 dilution; BD
513 Biosciences #550838), rabbit anti-H3K4me3 (1:500 dilution; Abcam #ab8580), and rabbit anti-
514 H3K36me3 (1:500 dilution; Abcam #ab9050). Primary antibodies were detected with Alexa Fluor
515 488-, 594-, or 647-conjugated secondary antibodies (1:500 dilution, Thermo Fisher Scientific #A-
516 11070, Abcam #ab150084, #ab150067, #ab150113, #ab150120, #ab150119, #ab150165, #ab150168,
517 and #ab150167) for 1 h at room temperature. The slides were washed with PBS several times and
518 mounted using VECTASHIELD medium with DAPI (Vector Laboratories, #H-1200). Immunolabeled

519 chromosome spreads were imaged by confocal microscopy using a Leica TCS SP5 resonant-scanning
520 confocal microscope. Projection images were then prepared using ImageJ Software (NIH, v. 1.6.0-65)
521 or Bitplane Imaris (v8.1) software.

522

523 **Immunoblotting**

524 To prepare protein extracts, tissues were collected from male C57BL/6 mice and lysed in TAP lysis
525 buffer (50 mM HEPES-KOH, pH 7.5, 100 mM KCl, 2 mM EDTA, 10% glycerol, 0.1% NP-40, 10
526 mM NaF, 0.25 mM Na₃VO₄ and 50 mM β-glycerolphosphate) plus protease inhibitors (Roche,
527 04693132001) for 30 min on ice, followed by centrifugation at 4°C at 13,000 × g for 15 min. The
528 supernatants were used for Western blotting. Equal amounts of protein were electrophoresed on 10%
529 Bis-Tris protein gels (Invitrogen, NP0315), and the bands were transferred to polyvinylidene fluoride
530 membranes (Millipore). The primary antibodies for immunoblotting included anti-tubulin (1:10,000
531 dilution; Proteintech Group, #11224-1-AP) and anti-ZCWPW1 (1:5,000 dilution; homemade).
532 Immunoreactive bands were detected and analyzed with a Bio-Rad ChemiDoc MP Imaging System
533 and Image Lab Software (Bio-Rad).

534

535 **ChIP-seq experiments**

536 The collected cells from testes were cross-linked in 100 μL of 1% formaldehyde in PBS at room
537 temperature for 10 min and this was followed by 25 μL of 1.25M glycine solution and mixing via
538 gentle tapping and incubation at room temperature for 5 min. After centrifugation, the cell pellet was
539 washed in PBS three times. Dynabeads Protein A beads (Life Technologies, 10001D) in a total
540 volume of 25 μL were washed twice with 200 μL ice-cold 140 mM RIPA buffer (10 mM Tris-HCl pH
541 7.5, 140 mM NaCl, 1 mM EDTA, 0.5 mM EGTA, 0.1% SDS, 0.1% Na-deoxycholate, 1% Triton X-
542 100, 1mM PMSF, 1×proteinase inhibitor Cocktail, and 20 mM Na-butyrate), followed by
543 resuspension in RIPA buffer to a final volume of 200 μL in a 1.5ml tube. A total volume of 5 μl
544 H3K4me3 antibody (Abcam, ab8580) or 7μl ZCWPW1 antibody (homemade, 5ug/μl) or 5μl
545 H3K36me3 antibody (Abcam, ab9050) was added to the beads suspension, and this was followed by

546 incubation on a tube rotator for at least 2.5 h at 4°C. The antibody-coated beads were then washed
547 twice in 140mM RIPA buffer, followed by resuspension with 200 µL 140mM RIPA buffer.

548 The cross-linked cells were incubated in 150 µL lysis buffer (50 mM Tris-HCl pH 8.0, 10 mM
549 EDTA pH8.0, 0.5% SDS, 1mM PMSF, 1× proteinase inhibitor cocktail, and 20 mM Na-butyrate) for
550 20 min on ice, then sonicated using a Diagenode Bioruptor sonication device for 23 cycles (30 s on
551 and then 30s off). A total volume of 150 µl 300 mM SDS-free RIPA buffer (10 mM Tris-HCl pH 7.5,
552 300 mM NaCl, 1 mM EDTA, 0.5 mM EGTA, 1% Triton X-100, 0.1% Na-deoxycholate, 1mM PMSF,
553 1× Cocktail proteinase inhibitor, and 20 mM Na-butyrate) and 200µl 140mM SDS-free RIPA buffer
554 were added to the samples. After centrifugation at 13,000 × g for 10 min at 4°C, 40 µL supernatant
555 was removed and used as the sample input. The remaining supernatant was transferred to a 1 ml tube
556 containing suspended antibody-coated Protein A beads, and this was followed by incubation on a tube
557 rotator overnight at 4°C.

558 For the H3K4me3 and H3K36me3 antibodies, the incubated Protein A beads were washed once
559 with RIPA buffer containing 250 mM NaCl, three times with RIPA buffer containing 500 mM NaCl,
560 and once with TE buffer (10 mM Tris-HCl pH 8.0, 1mM EDTA). For the ZCWPW1 antibody, the
561 incubated Protein A beads were washed twice with RIPA buffer containing 250 mM NaCl, once with
562 RIPA buffer containing 500mM NaCl, and once with TE buffer. Next, the beads were transferred to a
563 new 0.5ml tube and incubated in 100 µL ChIP elution buffer (10mM Tris-HCl pH8.0, 5mM EDTA,
564 300mM NaCl, 0.5% SDS) containing 5 µL proteinase K (Qiagen, 20mg/ml stock) at 55°C for 2 h and
565 then at 65°C for 4 h. The eluate was transferred to a 0.5 mL tube, and the enriched DNA was purified
566 by phenol–chloroform, followed by dissolution in 50 µL TE buffer.

567 An NEBNext Ultra II DNA Library Prep Kit for Illumina (NEB, E7645S) was used for library
568 construction according to the product's instructions. DNA was first end repaired and A-tailed by
569 adding 7 µL NEBNext Ultra II End Prep Reaction Buffer and 3 µL NEBNext Ultra II End Prep
570 Enzyme Mix. Samples were incubated at 20°C for 30min and then at 65°C for 30min, and finally
571 cooled to 4°C in a thermal cycler. Adaptor ligation was performed by adding 30 µL NEBNext Ultra II
572 Ligation Master Mix, 1 µL NEBNext Ligation Enhancer, 0.8 µL 200mM ATP, and 2.5 µL 15 µM
573 Illumina Multiplexing Adaptors. Samples were thoroughly mixed and incubated at 20°C for 40 min.

574 Following adaptor ligation, 1.2 volume SPRIselect beads (Beckman Coulter, B23318) were used to
575 purify the DNA. PCR amplification was performed with NEBNext Ultra II Q5 Master Mix. The PCR
576 cycle number was evaluated using a FlashGel™ System (Lonza, 57063). The volume of the PCR
577 product was adjusted to 100 µL by adding 50 µl TE buffer. The 300–700 bp DNA fragments were
578 selected with 0.5 volumes plus 0.5 volumes SPRIselect beads and then eluted in 20 µL water. The
579 libraries were sequenced on a HiSeq X-ten instrument set for paired-end 150 bp sequencing
580 (Illumina).

581

582 **ChIP-seq Bioinformatics Analysis**

583 The ChIP-seq raw reads were cropped to 100 bp, and the low quality reads were removed using
584 Trimmomatic v0.32 (Bolger et al., 2014). Paired reads were mapped to the mouse genome (version
585 mm10) by Bowtie2 v2.3.4.2 with the parameters “-X 2000 -no-discordant -no-contain” (Langmead
586 and Salzberg, 2012). Reads with low mapping quality (MAPQ < 10) and PCR duplicated reads were
587 removed by Samtools and Picard (DePristo et al., 2011; Li et al., 2009).

588 Reads of two replicates were merged to call the necessary peaks, while only one replicate of
589 H3K4me3 and H3K36me3 in Lam et al was used to call peaks in SCP3⁺/H1T⁻ spermatocytes using
590 relatively-stringent conditions. The H3K4me3 peaks in this work and in Lam *et al.* were called by
591 MACS2 v2.1.0 (Zhang et al., 2008) with the parameters “--SPMR -p 0.01 -nomodel” and “--SPMR -
592 nomodel -q 0.05 ”, the ZCWPW1 peaks were called with the parameters “ -SPMR -p 0.001 -
593 nomodel”, the H3K36me3 peaks in Grey *et al.* and Lam *et al.* were called with the parameters “ --
594 SPMR --broad -nomodel” and “--SPMR --broad -nomodel -p 0.001”, and the affinity-seq PRDM9
595 peaks in Walker *et al.* were called with the parameters “--SPMR -nomodel -p 0.05”. The peaks for
596 DMC1 and PRDM9 in Grey *et al.* were directly obtained from their published work (Grey et al.,
597 2017) and transformed to mm10 using the LiftOver application from UCSC. The SPO11 hotspots in
598 Lange et al were directly obtained from their published work (Lange et al., 2016). The peaks
599 intensities were denoted as the fold changes over input lambdas, which were obtained from the results
600 produced by MACS2 callpeak. ZCWPW1 and H3K4me3 (Lam *et al.*) peaks were further selected

601 based on peak intensities greater than a 3-fold enrichment over the input lambda. Affinity-seq PRDM9
602 peaks in Walker *et al.* and H3K36me3 peaks in Lam *et al.* were further selected based on peak
603 intensity greater than a 2-fold enrichment over the input lambda. The normalized signals of
604 H3K4me3, H3K36me3, ZCWPW1, PRDM9, and DMC1 were generated using MACS2 bdgcmp,
605 following the output produced by MACS2 callpeak with SPMR (reads per million for each covered
606 position). The FC over input lambda worked as the signal enrichment and was transformed into
607 Bigwig using bedGraphToBigWig. ChIP-seq signal tracks were visualized by Integrative Genomics
608 Viewer (Robinson *et al.*, 2011). The computeMatrix algorithm in Deeptools2 (Ramirez *et al.*, 2016)
609 was used to calculate the normalized signal of each 40bp-size bins in the regions of peak center \pm 2k
610 bp. Deeptools plotHeatmap, plotProfile and R (3.4.4) were used to generate the profile plot and
611 heatmap. The script findMotifsGenome.pl function in the HOMER software (Heinz *et al.*, 2010) was
612 used to examine the enrichment for transcription factor binding motifs. The gene-region association
613 was determined using the GREATER software (McLean *et al.*, 2010). The genomic regions including
614 promoters (TSS \pm 2k bp), exons, introns, intergenic regions, transposon elements, CpG islands, and
615 distal enhancers were downloaded from the UCSC Table Browser under the mm10 version.

616

617 **Spatial overlap of ZCWPW1 peaks with other regions**

618 The peak distribution over genome elements and the overlap between two types of peaks were
619 calculated using bedtools (v2.25.0). The random binding sites (peaks) used as a control were created
620 with the same number and size distribution as the observed peaks by using the regioneR package
621 version1.18.1 (Gel *et al.*, 2016) implemented in R. Using regioneR, a Monte Carlo permutation test
622 with 10,000 iterations was performed. In each iteration, the random binding sites were arbitrarily
623 shuffled in the mouse genome. From this shuffling, the average overlap and standard deviation of the
624 random binding site set was determined, as well as the statistical significance of the association
625 between ZCWPW1 binding sites.

626

627 **RNA-seq experiments and bioinformatics analysis**

628 The RNA was extracted from the testis with the Direct-zo RNA MiniPrep kit (Zymo). A total amount
629 of 1.5 µg RNA per sample was used as input material for the RNA sample preparations. Sequencing
630 libraries were generated using the NEBNext Ultra RNA Library Prep Kit for Illumina (NEB, USA)
631 following the manufacturer's recommendations. QC-passed libraries were sequenced on the
632 HiSeq X-ten instrument with the paired-end 150 bp.

633 The low-quality reads were removed using Trimmomatic v0.32 (Bolger et al., 2014). Paired reads
634 were mapped to the mouse genome (version mm10) by hisat2 v2.1.0 (Pertea et al., 2016) and to the
635 transcriptome by Salmon v 0.8.2. The DESeq2 v 1.18.0 software (Love et al., 2014) was used to
636 identify DEGs from the raw counts produced by Salmon with the two conditions: P adjust < 0.05, and
637 fold change ≥ 2 or fold change ≤ 0.5 . Metascape (Zhou et al., 2019) was used to perform Gene Ontology
638 analysis of DEGs.

639

640 **Statistical analysis**

641 Two-tailed Wilcoxon rank sum tests were performed to obtain inferential statistical significance (p
642 values) in related analyses by using the R function wilcox.test. No statistical methods were used to
643 predetermine sample size.

644

645 **Data availability**

646 All data generated or analyzed during this study are included in the manuscript and supporting files.
647 The raw sequencing data produced in this study (ChIP-seq data listed in Supplemental file1) and the
648 RNA-seq data have been deposited with the Genome Sequence Archive
649 (<https://bigd.big.ac.cn/gsa/s/CjpbIjf>) under accession number PRJCA001901.

650

651 **Author contributions**

652 Hongbin Liu, Zi-Jiang Chen, and Jiang Liu conceived and designed the entire project. Tao Huang
653 performed the ChIP-seq and immunofluorescence, analyzed and interpreted the data, and wrote and
654 edited the manuscript. Shenli Yuan performed the ChIP-seq and data analysis. Mengjing Li and
655 Xiaochen Yu performed immunofluorescence experiments and helped write and edit the manuscript.

656 Yingying Yin bred the mice and performed the Western blot. Chuanxin Zhang, Jianhong Zhang, and
657 Lei Gao provided guidance in ChIP-seq. Gang Lu, Chao Liu, and Wei Li helped design the mouse
658 knock-in model construction. Hongbin Liu, Zi-Jiang Chen, and Jiang Liu supervised the study and
659 edited the manuscript.

660

661 **Acknowledgments**

662 We are grateful for the interesting discussion with K. Liu from the University of Hong Kong, China,
663 in the very initial phase of the study. We thank Translational Medicine Core Facility of Shandong
664 University for consultation and instrument availability that supported this work and Jing Xin for
665 assistance with animal work (Reproductive Hospital Affiliated to Shandong University). This work
666 was supported by the Major Program of the National Natural Science Foundation of China
667 [31890780], the National Key Research and Development Programs of China [2018YFC1003400]
668 and the Young Scholars Program of Shandong University (2016WLJH50).

669

670 **Declaration of interests**

671 The authors declare no competing interests.

672

673 **References**

- 674 1. Handel MA and Schimenti JC. Genetics of mammalian meiosis: regulation,
675 dynamics and impact on fertility. *Nature reviews Genetics*. 2010; 11: 124-36.
676 doi:10.1038/nrg2723.
- 677 2. Bolcun-Filas E and Schimenti JC. Genetics of meiosis and recombination in
678 mice. *International review of cell and molecular biology*. 2012; 298: 179-227.
679 doi:10.1016/B978-0-12-394309-5.00005-5.
- 680 3. Hunter N. Meiotic Recombination: The Essence of Heredity. *Cold Spring*
681 *Harbor perspectives in biology*. 2015; 7. doi:10.1101/cshperspect.a016618.

- 682 4. Gray S and Cohen PE. Control of Meiotic Crossovers: From Double-Strand
683 Break Formation to Designation. *Annual review of genetics*. 2016; 50: 175-210.
684 doi:10.1146/annurev-genet-120215-035111.
- 685 5. Zickler D and Kleckner N. Recombination, Pairing, and Synapsis of Homologs
686 during Meiosis. *Cold Spring Harbor perspectives in biology*. 2015; 7.
687 doi:10.1101/cshperspect.a016626.
- 688 6. de Massy B. Initiation of meiotic recombination: how and where?
689 Conservation and specificities among eukaryotes. *Annual review of genetics*. 2013;
690 47: 563-99. doi:10.1146/annurev-genet-110711-155423.
- 691 7. Baudat F, Imai Y and de Massy B. Meiotic recombination in mammals:
692 localization and regulation. *Nature reviews Genetics*. 2013; 14: 794-806.
693 doi:10.1038/nrg3573.
- 694 8. Sun F, Fujiwara Y, Reinholdt LG, et al. Nuclear localization of PRDM9 and its
695 role in meiotic chromatin modifications and homologous synapsis. *Chromosoma*.
696 2015; 124: 397-415. doi:10.1007/s00412-015-0511-3.
- 697 9. Parvanov ED, Tian H, Billings T, et al. PRDM9 interactions with other proteins
698 provide a link between recombination hotspots and the chromosomal axis in meiosis.
699 *Molecular biology of the cell*. 2017; 28: 488-99. doi:10.1091/mbc.E16-09-0686.
- 700 10. Grey C, Baudat F and de Massy B. PRDM9, a driver of the genetic map.
701 *PLoS genetics*. 2018; 14: e1007479. doi:10.1371/journal.pgen.1007479.
- 702 11. Paigen K and Petkov PM. PRDM9 and Its Role in Genetic Recombination.
703 *Trends in genetics : TIG*. 2018; 34: 291-300. doi:10.1016/j.tig.2017.12.017.
- 704 12. Sommermeyer V, Beneut C, Chaplais E, Serrentino ME and Borde V. Spp1, a
705 member of the Set1 Complex, promotes meiotic DSB formation in promoters by
706 tethering histone H3K4 methylation sites to chromosome axes. *Molecular cell*. 2013;
707 49: 43-54. doi:10.1016/j.molcel.2012.11.008.
- 708 13. Acquaviva L, Szekvolgyi L, Dichtl B, et al. The COMPASS subunit Spp1 links
709 histone methylation to initiation of meiotic recombination. *Science*. 2013; 339: 215-8.
710 doi:10.1126/science.1225739.
- 711 14. Myers S, Bowden R, Tumian A, et al. Drive against hotspot motifs in primates
712 implicates the PRDM9 gene in meiotic recombination. *Science*. 2010; 327: 876-9.
713 doi:10.1126/science.1182363.

- 714 15. Parvanov ED, Petkov PM and Paigen K. Prdm9 controls activation of
715 mammalian recombination hotspots. *Science*. 2010; 327: 835.
716 doi:10.1126/science.1181495.
- 717 16. Baudat F, Buard J, Grey C, et al. PRDM9 is a major determinant of meiotic
718 recombination hotspots in humans and mice. *Science*. 2010; 327: 836-40.
719 doi:10.1126/science.1183439.
- 720 17. Brick K, Smagulova F, Khil P, Camerini-Otero RD and Petukhova GV. Genetic
721 recombination is directed away from functional genomic elements in mice. *Nature*.
722 2012; 485: 642-5. doi:10.1038/nature11089.
- 723 18. Powers NR, Parvanov ED, Baker CL, Walker M, Petkov PM and Paigen K.
724 The Meiotic Recombination Activator PRDM9 Trimethylates Both H3K36 and H3K4
725 at Recombination Hotspots In Vivo. *PLoS genetics*. 2016; 12: e1006146.
726 doi:10.1371/journal.pgen.1006146.
- 727 19. Diagouraga B, Clement JAJ, Duret L, Kadlec J, de Massy B and Baudat F.
728 PRDM9 Methyltransferase Activity Is Essential for Meiotic DNA Double-Strand Break
729 Formation at Its Binding Sites. *Molecular cell*. 2018; 69: 853-65 e6.
730 doi:10.1016/j.molcel.2018.01.033.
- 731 20. Grey C, Clement JA, Buard J, et al. In vivo binding of PRDM9 reveals
732 interactions with noncanonical genomic sites. *Genome research*. 2017; 27: 580-90.
733 doi:10.1101/gr.217240.116.
- 734 21. Bergerat A, de Massy B, Gadelle D, Varoutas PC, Nicolas A and Forterre P.
735 An atypical topoisomerase II from Archaea with implications for meiotic
736 recombination. *Nature*. 1997; 386: 414-7. doi:10.1038/386414a0.
- 737 22. Keeney S, Giroux CN and Kleckner N. Meiosis-specific DNA double-strand
738 breaks are catalyzed by Spo11, a member of a widely conserved protein family. *Cell*.
739 1997; 88: 375-84. doi:10.1016/s0092-8674(00)81876-0.
- 740 23. Robert T, Nore A, Brun C, et al. The TopoVIB-Like protein family is required
741 for meiotic DNA double-strand break formation. *Science*. 2016; 351: 943-9.
742 doi:10.1126/science.aad5309.
- 743 24. Vrielynck N, Chambon A, Vezon D, et al. A DNA topoisomerase VI-like
744 complex initiates meiotic recombination. *Science*. 2016; 351: 939-43.
745 doi:10.1126/science.aad5196.

- 746 25. Panizza S, Mendoza MA, Berlinger M, et al. Spo11-accessory proteins link
747 double-strand break sites to the chromosome axis in early meiotic recombination.
748 *Cell*. 2011; 146: 372-83. doi:10.1016/j.cell.2011.07.003.
- 749 26. Pittman DL, Cobb J, Schimenti KJ, et al. Meiotic prophase arrest with failure
750 of chromosome synapsis in mice deficient for Dmc1, a germline-specific RecA
751 homolog. *Molecular cell*. 1998; 1: 697-705. doi:10.1016/s1097-2765(00)80069-6.
- 752 27. Tarsounas M, Morita T, Pearlman RE and Moens PB. RAD51 and DMC1 form
753 mixed complexes associated with mouse meiotic chromosome cores and
754 synaptonemal complexes. *The Journal of cell biology*. 1999; 147: 207-20.
755 doi:10.1083/jcb.147.2.207.
- 756 28. Dai J, Voloshin O, Potapova S and Camerini-Otero RD. Meiotic Knockdown
757 and Complementation Reveals Essential Role of RAD51 in Mouse
758 Spermatogenesis. *Cell reports*. 2017; 18: 1383-94. doi:10.1016/j.celrep.2017.01.024.
- 759 29. Inagaki A, Schoenmakers S and Baarends WM. DNA double strand break
760 repair, chromosome synapsis and transcriptional silencing in meiosis. *Epigenetics*.
761 2010; 5: 255-66. doi:10.4161/epi.5.4.11518.
- 762 30. Keeney S, Lange J and Mohibullah N. Self-organization of meiotic
763 recombination initiation: general principles and molecular pathways. *Annual review*
764 *of genetics*. 2014; 48: 187-214. doi:10.1146/annurev-genet-120213-092304.
- 765 31. Lange J, Pan J, Cole F, Thelen MP, Jasin M and Keeney S. ATM controls
766 meiotic double-strand-break formation. *Nature*. 2011; 479: 237-40.
767 doi:10.1038/nature10508.
- 768 32. Garcia V, Gray S, Allison RM, Cooper TJ and Neale MJ. Tel1(ATM)-mediated
769 interference suppresses clustered meiotic double-strand-break formation. *Nature*.
770 2015; 520: 114-8. doi:10.1038/nature13993.
- 771 33. Baudat F and de Massy B. Regulating double-stranded DNA break repair
772 towards crossover or non-crossover during mammalian meiosis. *Chromosome*
773 *research : an international journal on the molecular, supramolecular and evolutionary*
774 *aspects of chromosome biology*. 2007; 15: 565-77. doi:10.1007/s10577-007-1140-3.
- 775 34. Kneitz B, Cohen PE, Avdievich E, et al. MutS homolog 4 localization to
776 meiotic chromosomes is required for chromosome pairing during meiosis in male
777 and female mice. *Genes & development*. 2000; 14: 1085-97.

- 778 35. Edlmann W, Cohen PE, Kneitz B, et al. Mammalian MutS homologue 5 is
779 required for chromosome pairing in meiosis. *Nature genetics*. 1999; 21: 123-7.
780 doi:10.1038/5075.
- 781 36. Yang F, Gell K, van der Heijden GW, et al. Meiotic failure in male mice lacking
782 an X-linked factor. *Genes & development*. 2008; 22: 682-91.
783 doi:10.1101/gad.1613608.
- 784 37. Lynn A, Soucek R and Borner GV. ZMM proteins during meiosis: crossover
785 artists at work. *Chromosome research : an international journal on the molecular,*
786 *supramolecular and evolutionary aspects of chromosome biology*. 2007; 15: 591-
787 605. doi:10.1007/s10577-007-1150-1.
- 788 38. Reynolds A, Qiao H, Yang Y, et al. RNF212 is a dosage-sensitive regulator of
789 crossing-over during mammalian meiosis. *Nature genetics*. 2013; 45: 269-78.
790 doi:10.1038/ng.2541.
- 791 39. Li M, Huang T, Li MJ, et al. The histone modification reader ZCWPW1 is
792 required for meiosis prophase I in male but not in female mice. *Science advances*.
793 2019a; 5: eaax1101. doi:10.1126/sciadv.aax1101.
- 794 40. Perry J and Zhao Y. The CW domain, a structural module shared amongst
795 vertebrates, vertebrate-infecting parasites and higher plants. *Trends in biochemical*
796 *sciences*. 2003; 28: 576-80. doi:10.1016/j.tibs.2003.09.007.
- 797 41. Liu Y, Tempel W, Zhang Q, et al. Family-wide Characterization of Histone
798 Binding Abilities of Human CW Domain-containing Proteins. *The Journal of biological*
799 *chemistry*. 2016; 291: 9000-13. doi:10.1074/jbc.M116.718973.
- 800 42. He F, Umehara T, Saito K, et al. Structural insight into the zinc finger CW
801 domain as a histone modification reader. *Structure*. 2010; 18: 1127-39.
802 doi:10.1016/j.str.2010.06.012.
- 803 43. Hoppmann V, Thorstensen T, Kristiansen PE, et al. The CW domain, a new
804 histone recognition module in chromatin proteins. *The EMBO journal*. 2011; 30:
805 1939-52. doi:10.1038/emboj.2011.108.
- 806 44. Smagulova F, Gregoret IV, Brick K, Khil P, Camerini-Otero RD and
807 Petukhova GV. Genome-wide analysis reveals novel molecular features of mouse
808 recombination hotspots. *Nature*. 2011; 472: 375-8. doi:10.1038/nature09869.
- 809 45. Segurel L. The complex binding of PRDM9. *Genome biology*. 2013; 14: 112.
810 doi:10.1186/gb-2013-14-1-112

- 811 10.1186/gb-2013-14-4-112.
- 812 46. Billings T, Parvanov ED, Baker CL, Walker M, Paigen K and Petkov PM. DNA
813 binding specificities of the long zinc-finger recombination protein PRDM9. *Genome*
814 *biology*. 2013; 14: R35. doi:10.1186/gb-2013-14-4-r35.
- 815 47. Walker M, Billings T, Baker CL, et al. Affinity-seq detects genome-wide
816 PRDM9 binding sites and reveals the impact of prior chromatin modifications on
817 mammalian recombination hotspot usage. *Epigenetics & chromatin*. 2015; 8: 31.
818 doi:10.1186/s13072-015-0024-6.
- 819 48. Khil PP, Smagulova F, Brick KM, Camerini-Otero RD and Petukhova GV.
820 Sensitive mapping of recombination hotspots using sequencing-based detection of
821 ssDNA. *Genome research*. 2012; 22: 957-65. doi:10.1101/gr.130583.111.
- 822 49. Stanzione M, Baumann M, Papanikos F, et al. Meiotic DNA break formation
823 requires the unsynapsed chromosome axis-binding protein IHO1 (CCDC36) in mice.
824 *Nature cell biology*. 2016; 18: 1208-20. doi:10.1038/ncb3417.
- 825 50. Tesse S, Bourbon HM, Debuchy R, et al. Asy2/Mer2: an evolutionarily
826 conserved mediator of meiotic recombination, pairing, and global chromosome
827 compaction. *Genes & development*. 2017; 31: 1880-93.
828 doi:10.1101/gad.304543.117.
- 829 51. Kumar R, Oliver C, Brun C, et al. Mouse REC114 is essential for meiotic DNA
830 double-strand break formation and forms a complex with MEI4. *Life science alliance*.
831 2018; 1: e201800259. doi:10.26508/lsa.201800259.
- 832 52. Wahls WP. Meiotic recombination hotspots: shaping the genome and insights
833 into hypervariable minisatellite DNA change. *Current topics in developmental*
834 *biology*. 1998; 37: 37-75. doi:10.1016/s0070-2153(08)60171-4.
- 835 53. Blat Y, Protacio RU, Hunter N and Kleckner N. Physical and functional
836 interactions among basic chromosome organizational features govern early steps of
837 meiotic chiasma formation. *Cell*. 2002; 111: 791-802. doi:10.1016/s0092-
838 8674(02)01167-4.
- 839 54. Adams-Cioaba MA and Min J. Structure and function of histone methylation
840 binding proteins. *Biochemistry and cell biology = Biochimie et biologie cellulaire*.
841 2009; 87: 93-105. doi:10.1139/O08-129.

- 842 55. Eidahl JO, Crowe BL, North JA, et al. Structural basis for high-affinity binding
843 of LEDGF PWWP to mononucleosomes. *Nucleic acids research*. 2013; 41: 3924-36.
844 doi:10.1093/nar/gkt074.
- 845 56. Rondelet G, Dal Maso T, Willems L and Wouters J. Structural basis for
846 recognition of histone H3K36me3 nucleosome by human de novo DNA
847 methyltransferases 3A and 3B. *Journal of structural biology*. 2016; 194: 357-67.
848 doi:10.1016/j.jsb.2016.03.013.
- 849 57. Vezzoli A, Bonadies N, Allen MD, et al. Molecular basis of histone H3K36me3
850 recognition by the PWWP domain of Brpf1. *Nature structural & molecular biology*.
851 2010; 17: 617-9. doi:10.1038/nsmb.1797.
- 852 58. Mahgoub M, Paiano J, Bruno M, et al. Dual Histone Methyl Reader ZCWPW1
853 Facilitates Repair of Meiotic Double Strand Breaks. *BioRxiv*. preprint first posted
854 online Oct. 29, 2019. doi:10.1101/821603.
- 855 59. Hinch AG, Zhang G, Becker PW, et al. Factors influencing meiotic
856 recombination revealed by whole-genome sequencing of single sperm. *Science*.
857 2019; 363. doi:10.1126/science.aau8861.
- 858 60. Li R, Bitoun E, Altemose N, Davies RW, Davies B and Myers SR. A high-
859 resolution map of non-crossover events reveals impacts of genetic diversity on
860 mammalian meiotic recombination. *Nature communications*. 2019b; 10: 3900.
861 doi:10.1038/s41467-019-11675-y.
- 862 61. Wells D, Bitoun E, Moralli D, et al. ZCWPW1 is recruited to recombination
863 hotspots by PRDM9, and is essential for meiotic double strand break repair. *BioRxiv*.
864 preprint first posted online Oct. 30, 2019. doi:10.1101/821678.
- 865 62. Peters AH, Plug AW, van Vugt MJ and de Boer P. A drying-down technique
866 for the spreading of mammalian meiocytes from the male and female germline.
867 *Chromosome research : an international journal on the molecular, supramolecular*
868 *and evolutionary aspects of chromosome biology*. 1997; 5: 66-8.
869 doi:10.1023/a:1018445520117.
- 870 63. Bolger AM, Lohse M and Usadel B. Trimmomatic: a flexible trimmer for
871 Illumina sequence data. *Bioinformatics*. 2014; 30: 2114-20.
872 doi:10.1093/bioinformatics/btu170.
- 873 64. Langmead B and Salzberg SL. Fast gapped-read alignment with Bowtie 2.
874 *Nature methods*. 2012; 9: 357-9. doi:10.1038/nmeth.1923.

- 875 65. DePristo MA, Banks E, Poplin R, et al. A framework for variation discovery
876 and genotyping using next-generation DNA sequencing data. *Nature genetics*. 2011;
877 43: 491-8. doi:10.1038/ng.806.
- 878 66. Li H, Handsaker B, Wysoker A, et al. The Sequence Alignment/Map format
879 and SAMtools. *Bioinformatics*. 2009; 25: 2078-9. doi:10.1093/bioinformatics/btp352.
- 880 67. Zhang Y, Liu T, Meyer CA, et al. Model-based analysis of ChIP-Seq (MACS).
881 *Genome biology*. 2008; 9: R137. doi:10.1186/gb-2008-9-9-r137.
- 882 68. Robinson JT, Thorvaldsdottir H, Winckler W, et al. Integrative genomics
883 viewer. *Nature biotechnology*. 2011; 29: 24-6. doi:10.1038/nbt.1754.
- 884 69. Ramirez F, Ryan DP, Gruning B, et al. deepTools2: a next generation web
885 server for deep-sequencing data analysis. *Nucleic acids research*. 2016; 44: W160-
886 5. doi:10.1093/nar/gkw257.
- 887 70. Heinz S, Benner C, Spann N, et al. Simple combinations of lineage-
888 determining transcription factors prime cis-regulatory elements required for
889 macrophage and B cell identities. *Molecular cell*. 2010; 38: 576-89.
890 doi:10.1016/j.molcel.2010.05.004.
- 891 71. Zhou Y, Zhou B, Pache L, et al. Metascape provides a biologist-oriented
892 resource for the analysis of systems-level datasets. *Nature communications*. 2019;
893 10: 1523. doi:10.1038/s41467-019-09234-6.
- 894 72. McLean CY, Bristor D, Hiller M, et al. GREAT improves functional
895 interpretation of cis-regulatory regions. *Nature biotechnology*. 2010; 28: 495-501.
896 doi:10.1038/nbt.1630.
- 897 73. Qin S, Min J, et al. Structure and function of the nucleosome-binding PWWP
898 domain. *Trends Biochem. Sci.* 2019; 39, 536-547
- 899 74. Lange J, Yamada S, Tischfield T, et al. The Landscape of Mouse Meiotic
900 Double-Strand Break Formation, Processing, and Repair. *Cell*. 2016; 167(3):695-708.
901 doi: 10.1016/j.cell.2016.09.035.
- 902 75. Gel B, Díez-Villanueva A, Serra E, et al. regioneR: an R/Bioconductor
903 package for the association analysis of genomic regions based on permutation tests.
904 *Bioinformatics*. 2016;32(2):289-91. doi: 10.1093/bioinformatics/btv562
- 905 76. Pertea M, Kim D, Pertea GM, et al. Transcript-level expression analysis of
906 RNA-seq experiments with HISAT, StringTie and Ballgown. *Nat Protoc*.
907 2016;11(9):1650-67. doi: 10.1038/nprot.2016.095.

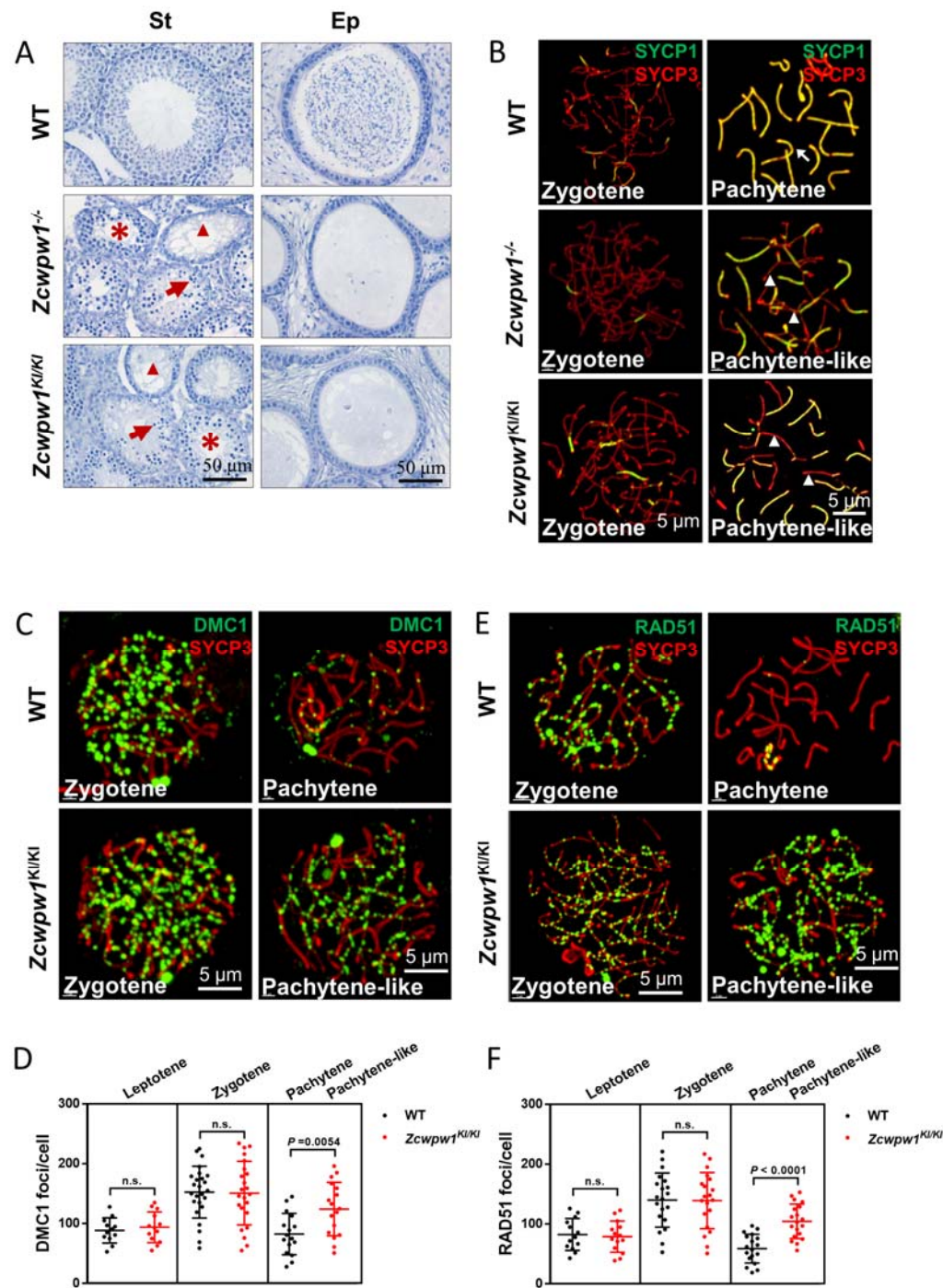
- 908 77. Love MI, Huber W, Anders S. Moderated estimation of fold change and
909 dispersion for RNA-seq data with DESeq2. *Genome Biol.* 2014;15(12):550. doi:
910 10.1186/s13059-014-0550-8
- 911 78. Zhou Y, Zhou B, Pache L, et al. Metascape provides a biologist-oriented
912 resource for the analysis of systems-level datasets. *Nat Commun.* 2019;10(1):1523.
913 doi: 10.1038/s41467-019-09234-6.
- 914 79. Davies B, Hatton, Altemose N, Hussin JG, et al. Re-engineering the zinc
915 fingers of PRDM9 reverses hybrid sterility in mice. *Nature.* 2016;530(7589):171-176.
916 doi: 10.1038/nature16931.

917

918

919

920 **Figure legends**

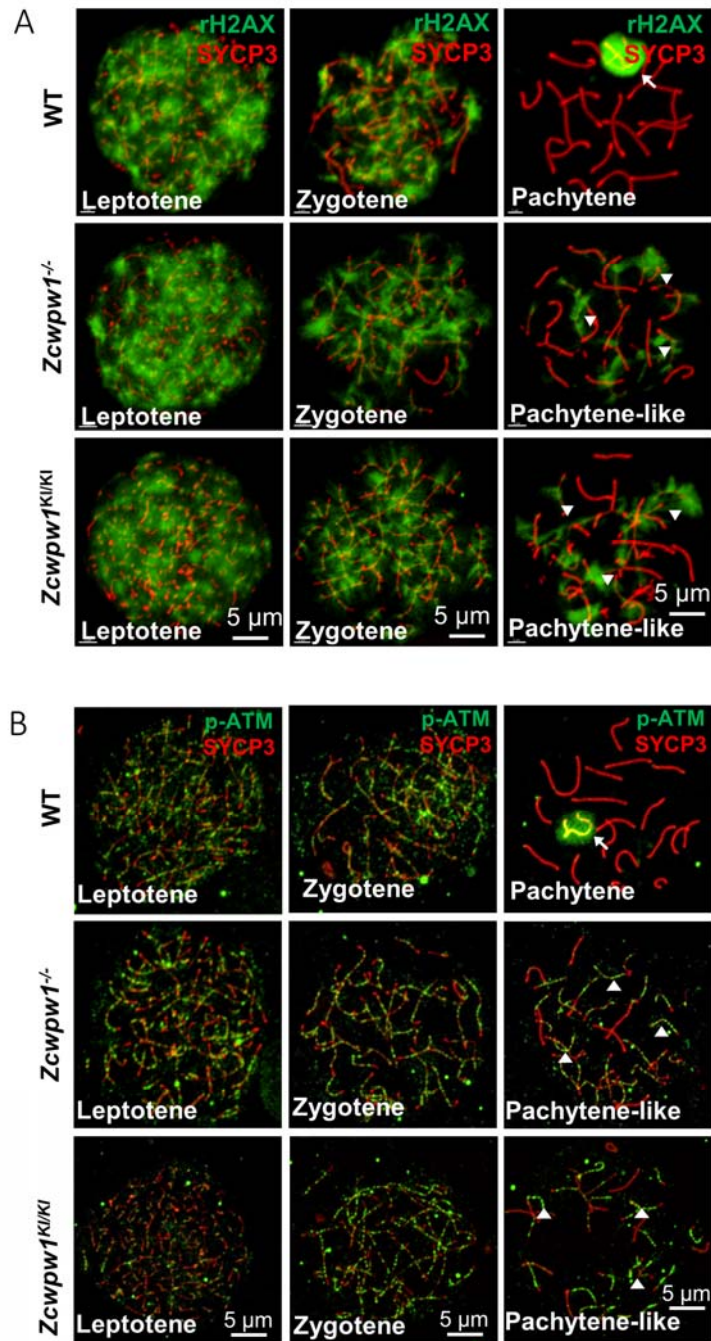


921

922 **Figure 1 The H3K4me3 reader function of ZCWPW1 is required for synapsis and meiotic**
 923 **recombination**

924 (A). Hematoxylin staining of adult C57BL/6 wild type, *Zcwpw1*^{-/-}, and *Zcwpw1*^{KI/KI} testes (left panel)
 925 and epididymides (right panel). Adult *Zcwpw1*^{-/-} and *Zcwpw1*^{KI/KI} testis sections showed near
 926 complete arrest of spermatogenesis. Arrows, apoptotic spermatocytes; arrowheads, empty

927 seminiferous tubules; asterisks, seminiferous tubules lacking post-meiotic spermatocytes. The
928 spermatogenic arrest led to empty epididymides in adult *Zcwpw1*^{-/-} and *Zcwpw1*^{KI/KI} mice. (St)
929 Seminiferous tubules, (Ep) Epididymides. **(B)**. Chromosome spreads of spermatocytes from the testes
930 of adult WT (upper panel), *Zcwpw1*^{-/-} (middle panel), and *Zcwpw1*^{KI/KI} (lower panel) males were
931 immunostained for the SC marker proteins SYCP1 (green) and SYCP3 (red). The arrow indicates a
932 pachytene spermatocyte in WT mice, with completely synapsed chromosomes, and the arrowheads
933 indicate the pachytene-like spermatocytes in adult *Zcwpw1*^{-/-} and *Zcwpw1*^{KI/KI} mice with
934 incompletely synapsed chromosomes. **(C)**. Chromosome spreads of spermatocytes from the testes of
935 adult WT and *Zcwpw1*^{KI/KI} males were immunostained for DMC1 (green) and SYCP3 (red).
936 Representative images of spermatocytes at zygotene and pachytene in WT and at zygotene and
937 pachytene-like stages in *Zcwpw1*^{KI/KI} are shown. **(D)**. Each dot represents the number of DMC1 foci
938 per cell, with black dots indicating WT spermatocytes and red dots indicating *Zcwpw1*^{KI/KI}
939 spermatocytes. Solid lines show the mean and SD of foci number in each group of spermatocytes. P
940 values were calculated by Student's t-test. **(E)**. Chromosome spreads of spermatocytes from the testes
941 of adult WT and *Zcwpw1*^{KI/KI} males immunostained for RAD51 (green) and SYCP3 (red). **(F)**. Each
942 dot represents the number of RAD51 foci per cell, with black dots indicating WT spermatocytes and
943 red dots indicating *Zcwpw1*^{KI/KI} spermatocytes. Solid lines show the mean and SD of the foci number
944 for each group of spermatocytes. P values were calculated by Student's t test. All experiments were
945 performed on adult mice (6-8weeks) with n > 3 for each genotype.

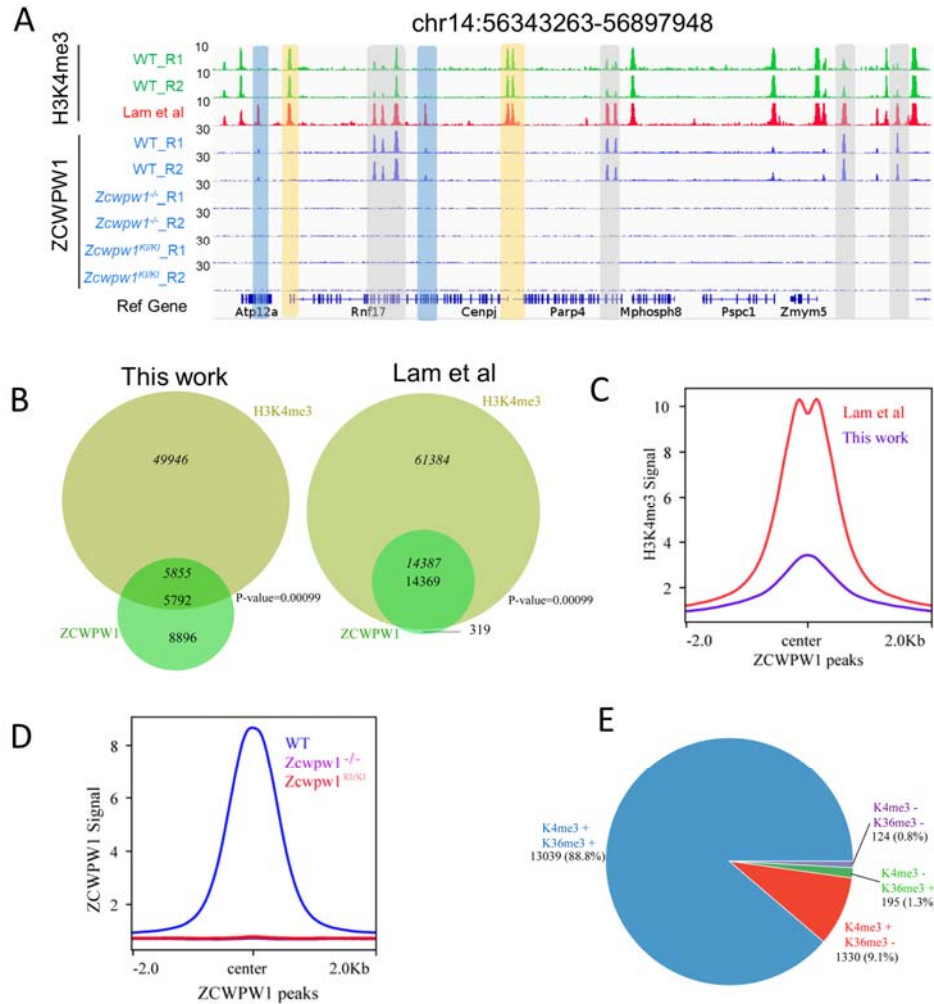


946

947 **Figure 2. The H3K4me3 reader function of ZCWPW1 is required for DSB repair**

948 (A). Chromosome spreads of spermatocytes from the testes of adult WT, *Zcwpw1*^{-/-}, and *Zcwpw1*^{Kl/Kl}
949 males immunostained for the DSB marker γ H2AX (green) and SYCP3 (red). (B). Chromosome
950 spreads of spermatocytes from the testes of adult WT, *Zcwpw1*^{-/-}, and *Zcwpw1*^{Kl/Kl} males
951 immunostained for the DSB repair protein p-ATM (green) and SYCP3 (red). Representative images

952 are shown for spermatocytes at the leptotene, zygotene, pachytene (arrow indicates the XY body), and
 953 pachytene-like (arrowheads indicate the p-ATM signal) stages of the three genotypes. All experiments
 954 were performed on adult mice (6-8weeks) with $n > 3$ for each genotype.



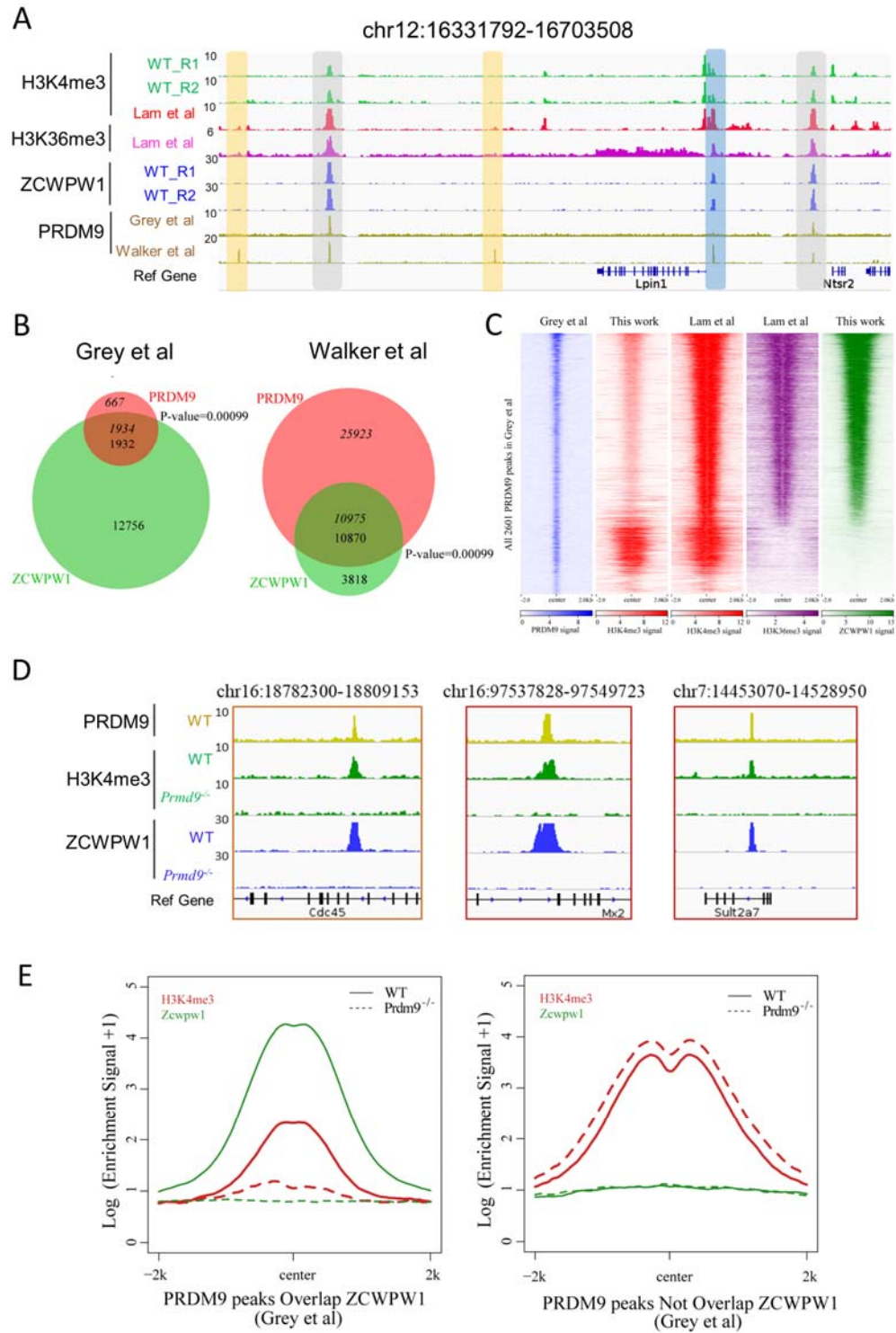
955

956 **Figure 3. ZCWPW1 is an H3K4me3 reader**

957 (A). ChIP-seq genome snapshot of the distribution of H3K4me3 and ZCWPW1 peaks in C57BL/6
 958 WT, *Zcwpw1*^{-/-}, and *Zcwpw1*^{KI/KI} mice along a 554-kb region of chromosome 14. H3K4me3 and
 959 ZCWPW1 signals were normalized (See Methods). Overlapping regions are indicated by grey or blue
 960 shaded areas, while non-overlapping regions of interest are indicated by orange shaded areas. R1 and
 961 R2 represent two independent replicates. The H3K4me3 tract (red) was generated with isolated stage-
 962 specific spermatocyte nuclei (Lam et al., 2019) (B). Venn diagram showing the overlap between
 963 ZCWPW1 peaks and H3K4me3 peaks. H3K4me3 data generated in whole testes (left, this study)

964 compared with H3K4me3 data generated with isolated stage-specific (SCP3⁺H1T⁻) spermatocyte
965 nuclei (right, Lam *et al.*). Italics (*14,387*) indicates the number of H3K4me3 peaks overlapping
966 ZCWPW1, while standard font (*14,369*) indicates the number of ZCWPW1 peaks overlapping with
967 H3K4me3 marks. P-values were calculated by using the permTest (see Methods, ntimes=1000). (C).
968 Profile plot of averaged normalized H3K4me3 signals (see Methods) in ZCWPW1 peaks obtained in
969 this work and in Lam *et al.* The profile shows the average values over 4-kb intervals for all 14,688
970 detected peaks (binding sites).

971 (D). Profile plot of the averaged ZCWPW1 signal in 14,688 ZCWPW1 peaks, in C57BL/6 WT,
972 *Zcwpw1*^{-/-} and *Zcwpw1*^{K1/K1} mice. (E). Pie chart showing the ratio of four ZCWPW1 peak groups
973 determined by their overlap with histone modification peaks generated with isolated stage-specific
974 spermatocyte nuclei (Lam *et al.*). The “+” indicates overlap, while “-” indicates no overlap. All
975 ChIP-seq experiments were performed in PD14 mice with n > 3 for each genotype.

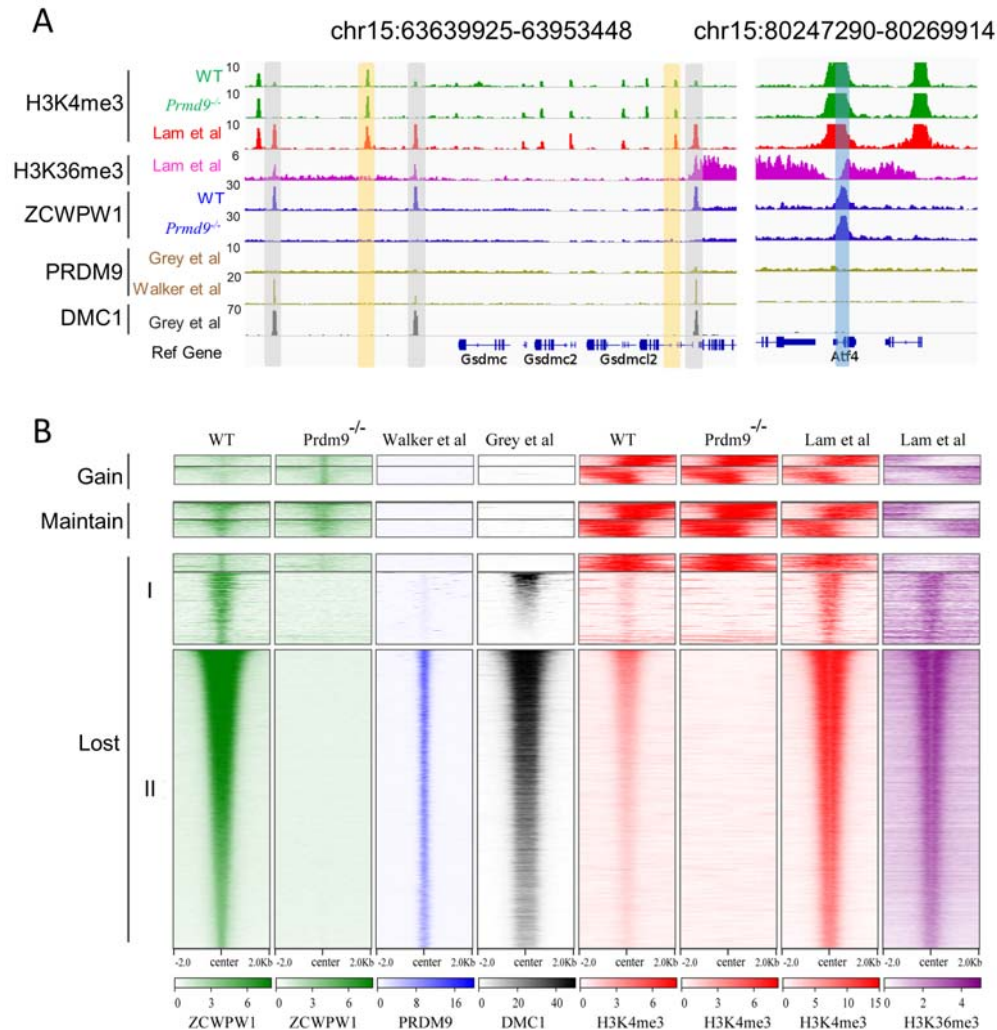


976

977 **Figure 4. ZCWPW1 binding is strongly promoted by the histone modification activity of**

978 **PRDM9**

979 (A). ChIP-seq genome snapshot of the distribution of H3K4me3, H3K36me3, ZCWPW1, and
980 PRDM9 peaks in C57BL/6 mice along a 372-kb region of chromosome 12. Overlapping peaks in
981 samples from all four analyses are indicated by grey or blue shaded areas, while non-overlapping
982 regions of interest are indicated by orange shaded areas. (B). Venn diagram showing the overlap
983 between PRDM9 peaks and ZCWPW1 binding sites. On the left are *in vivo* PRDM9 data generated
984 by Grey *et al.* (2018), while on the right are *in vitro* affinity-seq PRDM9 data generated by Walker *et*
985 *al.* (2015). Italics indicate PRDM9 peak overlap with ZCWPW1, while standard font indicates
986 ZCWPW1 peak overlap with PRDM9 peaks. (C). Heatmap showing the correlation among H3K4me3,
987 H3K36me3, and ZCWPW1 with PRDM9 peaks (Grey *et al.* 2018). Each row represents a PRDM9
988 binding site of ± 2 kb around the center and ranked by ZCWPW1 signal from the highest to the lowest.
989 Color indicates normalized ChIP-seq signal (See Methods). (D). ChIP-seq genome snapshot showing
990 changes in H3K4me3 and ZCWPW1 binding distributions following *Prdm9* knockout (*Prdm9*^{-/-})
991 along a 27/12-kb region of chromosome 16 and a 76-kb region of chromosome 7. The PRDM9 data
992 were obtained from Grey *et al.* (2018). (E). Profile plot of averaged H3K4me3 and ZCWPW1 signals
993 obtained in this work with two types of PRDM9 peaks (Grey *et al.*, 2018) following *Prdm9* knockout.
994 The Y-axis shows log base-2 transformation of the normalized signal. All ChIP-seq experiments were
995 performed using PD14 mice with $n > 3$ for each genotype.



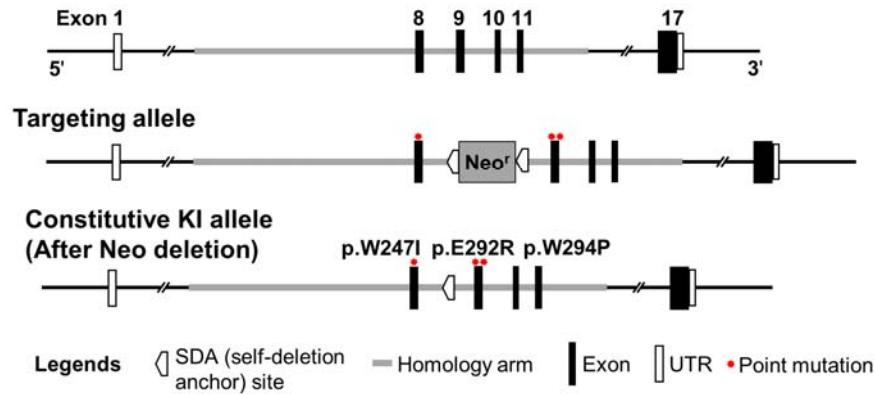
996

997 **Figure 5. ZCWPW1 localizes to DMC1-labelled DSB hotspots in a PRDM9-dependent manner**

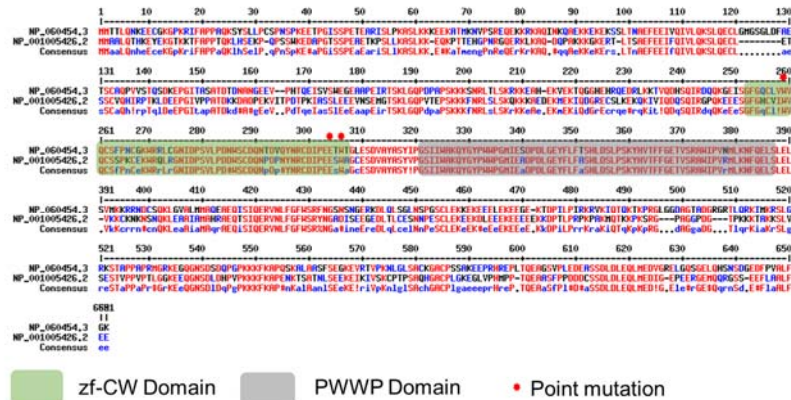
998 (A). ChIP-seq genome snapshot of the distribution of H3K4me3, H3K36me3, ZCWPW1, PRDM9,
 999 and DMC1 peaks in C57BL/6 mice with changes in H3K4me3 and ZCWPW1 binding sites in *Prdm9*
 1000 knockout mice. ZCWPW1 and DMC1 overlapping regions are indicated by grey shaded areas, while
 1001 non-overlapping regions of interest are indicated by orange or blue shaded areas. (B). Heatmap
 1002 showing PRDM9 (Walker *et al*), DMC1 (Grey *et al*), H3K4me3 (Lam *et al*), H3K36me3 (Lam *et al*),
 1003 H3K4me3 (WT and *Prdm9*^{-/-}), and ZCWPW1 (WT and *Prdm9*^{-/-}) corresponding with Gained, Lost,
 1004 or Maintained groups of ZCWPW1 peaks (also see Figure 4–figure supplement 3A). Lost Group I
 1005 represents ZCWPW1 peaks not overlapping with PRDM9 affinity-Seq peaks that were lost in *Prdm9*
 1006 knockout mice, and Lost Group II represents ZCWPW1 peaks overlapping with PRDM9 affinity-Seq

1007 peaks that were lost in *Prdm9* knockout mice. All ChIP-seq experiments were performed using PD14
 1008 mice with $n > 3$ for each genotype.

A *Zcwpw1* Wildtype Allele



B



C *Prdm9* Mutant Allele

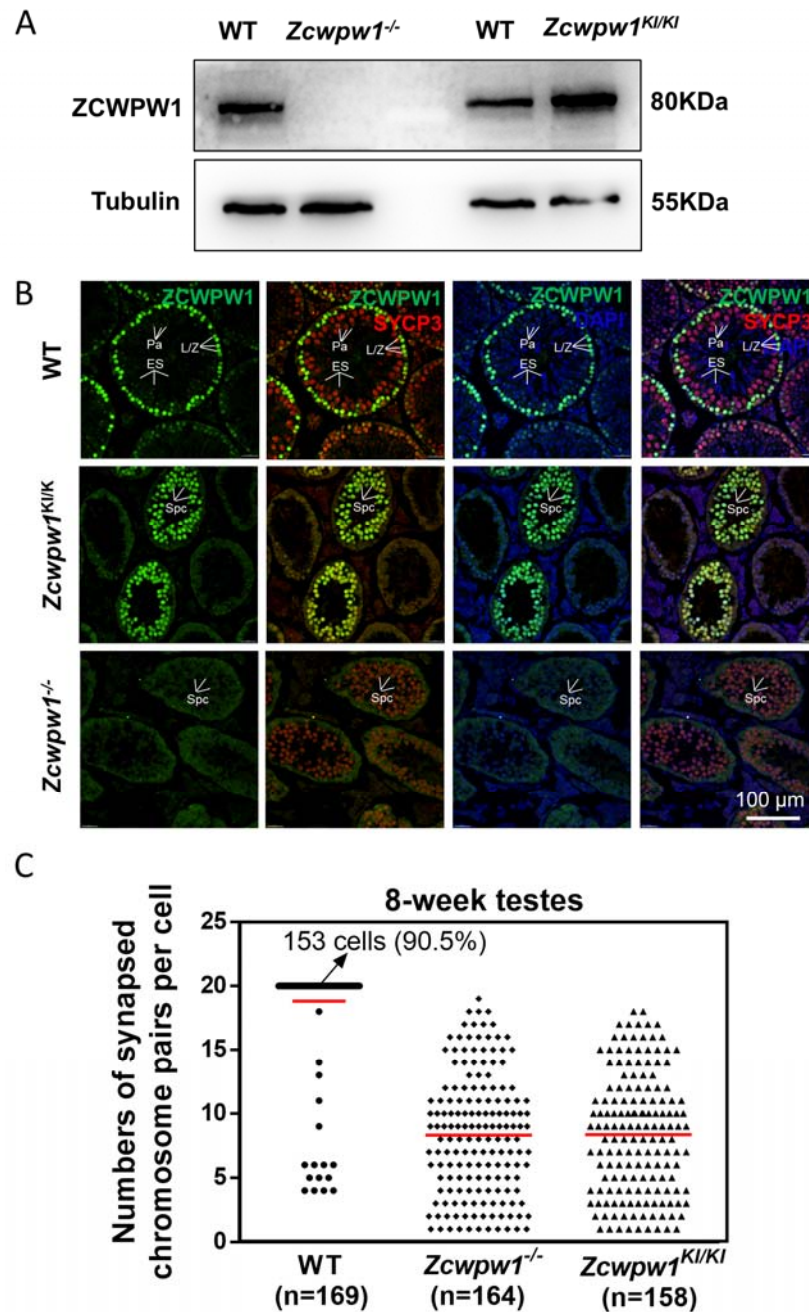


1009

1010 **Figure 1–figure supplement 1. Generation of *Zcwpw1* reader-dead-mutant mice and *Prdm9***
 1011 **knockout mice**

1012 (A). Schematic representation of the genome editing strategy to generate knock-in *Zcwpw1* reader-
 1013 dead-mutant mice. (B). Sequence alignment of human ZCWPW1 (NP_060454.3) and mouse
 1014 ZCWPW1 (NP_001005426.2). Conserved regions of ZCWPW1 are indicated by green shaded areas
 1015 for the zf-CW domain and grey shaded areas for the PWWP domain. Red asterisks indicate the point

1016 mutation sites. (C). Schematic representation of the CRISP-cas9 genome editing strategy used to
 1017 generate the *Prdm9* knockout mice showing the gRNAs (arrows), the corresponding coding exons
 1018 (black and red thick lines), and the non-coding exons (gray thick lines). Red thick lines (coding exons)
 1019 represent approximately 12,000 bp deleted from the wild-type *Prdm9* allele.

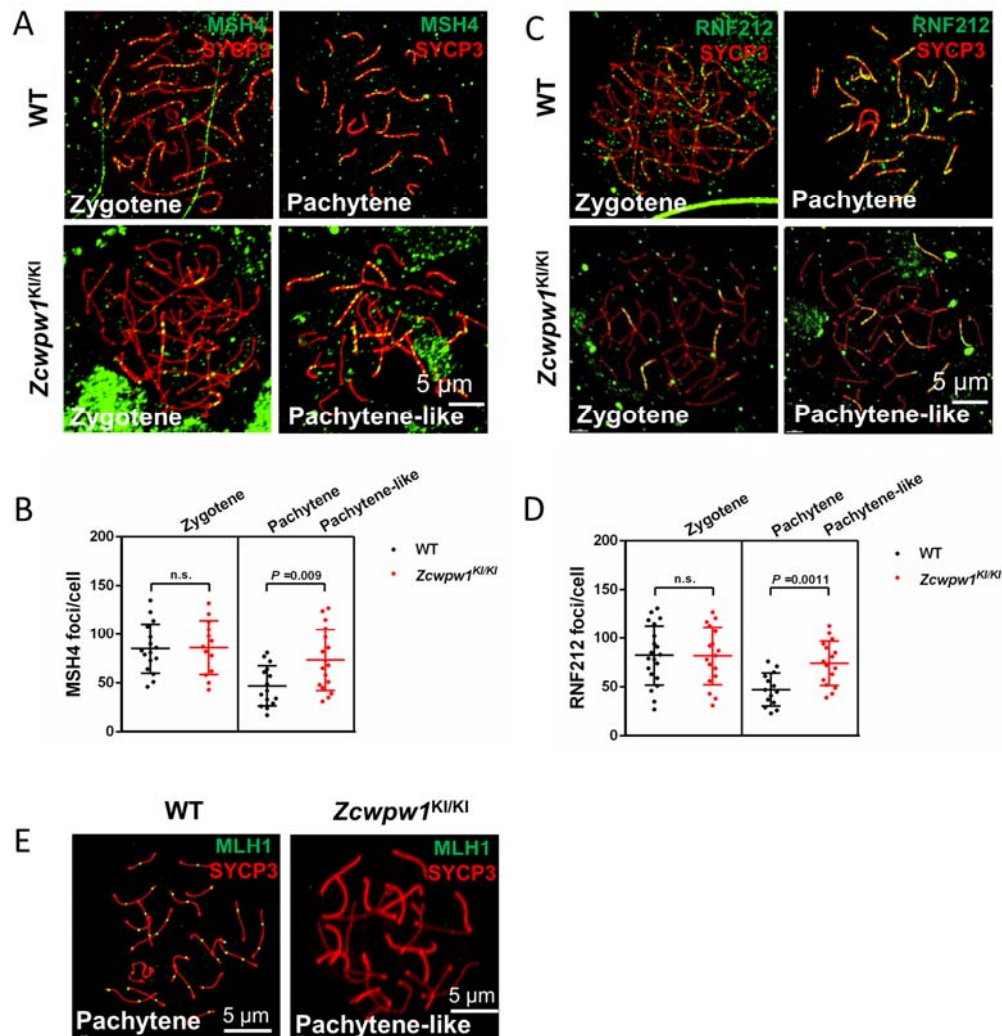


1020

1021 **Figure 1–figure supplement 2. Distribution pattern of ZCWPW1 in WT, *Zcwpw1*^{Kl/Kl} and**

1022 *Zcwpw1*^{-/-} mice

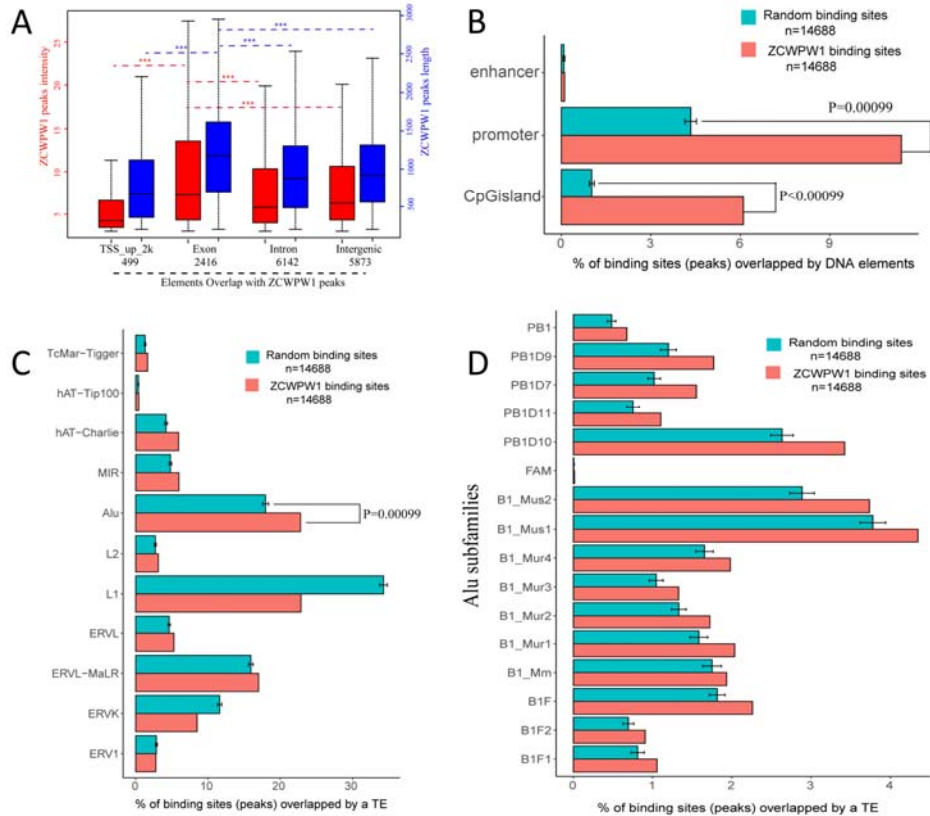
1023 (A). Western blots showing that ZCWPW1 was not detected in *Zcwpw1*^{-/-} testes but was present in
 1024 WT testes, and with a similarly intense signal for *Zcwpw1*^{K1/K1}. Tubulin was used as the loading
 1025 control. The experiments were performed using PD20 mice with n>3 for each genotype. (B).
 1026 Immunofluorescence staining of ZCWPW1 and SYCP3 in WT, *Zcwpw1*^{K1/K1} and *Zcwpw1*^{-/-}
 1027 histological cross-sections. DNA was stained with DAPI. Abbreviations: L/Z, leptotene/zygotene
 1028 spermatocytes; Pa, pachytene spermatocytes; Spc, spermatocytes; ES, elongated spermatids; (C). The
 1029 numbers of synapsed chromosome pairs in WT, *Zcwpw1*^{-/-} and *Zcwpw1*^{K1/K1} spermatocytes. In
 1030 *Zcwpw1*^{-/-} and *Zcwpw1*^{K1/K1} spermatocytes, the average number of synapsed chromosome pairs was 8.
 1031 All experiments were performed on adult mice (6–8 weeks old) with n > 3 for each genotype.



1032

1033 **Figure 1–figure supplement 3. Meiotic recombination defects in *Zcwpw1* knock-in mice**

1034 (A). Chromosome spreads of spermatocytes from the testes of adult WT and *Zcwpw1*^{K1/K1} males
1035 immunostained for the recombination factor MSH4 (green) and SYCP3 (red). (B). Each dot
1036 represents the number of MSH4 foci per cell. Black dots indicate WT spermatocytes, and red dots
1037 indicate *Zcwpw1*^{K1/K1} spermatocytes. Solid lines show the mean and SD of foci in each group of
1038 spermatocytes. P-values were calculated by Student's t-test. (C). Chromosome spreads of
1039 spermatocytes from WT and *Zcwpw1*^{K1/K1} males immunostained for the recombination factor RNF212
1040 (green) and SYCP3 (red). Representative images are shown for spermatocytes at the zygotene,
1041 pachytene, and pachytene-like stages of the three genotypes. (D). Each dot represents the number of
1042 RNF212 foci per cell, with black dots indicating WT spermatocytes and red dots indicating
1043 *Zcwpw1*^{K1/K1} spermatocytes. Solid lines show the mean and SD of foci number for each group of
1044 spermatocytes. P-values were calculated by Student's t-test. (E). Chromosome spreads of
1045 spermatocytes from the testes of adult WT and *Zcwpw1*^{K1/K1} males immunostained for MLH1 (green)
1046 and SYCP3 (red). Representative images are shown for spermatocytes at the pachytene stage in WT
1047 and the pachytene-like stage in *Zcwpw1*^{K1/K1}. All experiments were performed on adult mice
1048 (6–8weeks old) with n > 3 for each genotype.



1049

1050 **Figure 3–figure supplement 1. Genome-wide properties of ZCWPW1-associated binding sites**

1051 (A). The distribution of ZCWPW1 peak intensity and peak length by location in genomic elements.

1052 (***P < 0.001 by two-tailed Wilcoxon rank sum test). The red boxplots and left Y-axis indicate peak

1053 intensity, while the blue boxplots and right Y-axis indicate peak length. (B). Percentage of ZCWPW1

1054 binding sites (peaks) overlapping with DNA elements compared with the random binding sites

1055 obtained by random shuffling of the identified ZCWPW1 binding sites. The X-axis indicates the

1056 percentage of binding sites overlapping with DNA elements. The random groups and P-values were

1057 generated using permTest, an R function in the regioneR package (see Methods, ntimes=1000). The

1058 barplot height of the random group represents the means of 1000 tests. Bars represent ± SD. (C).

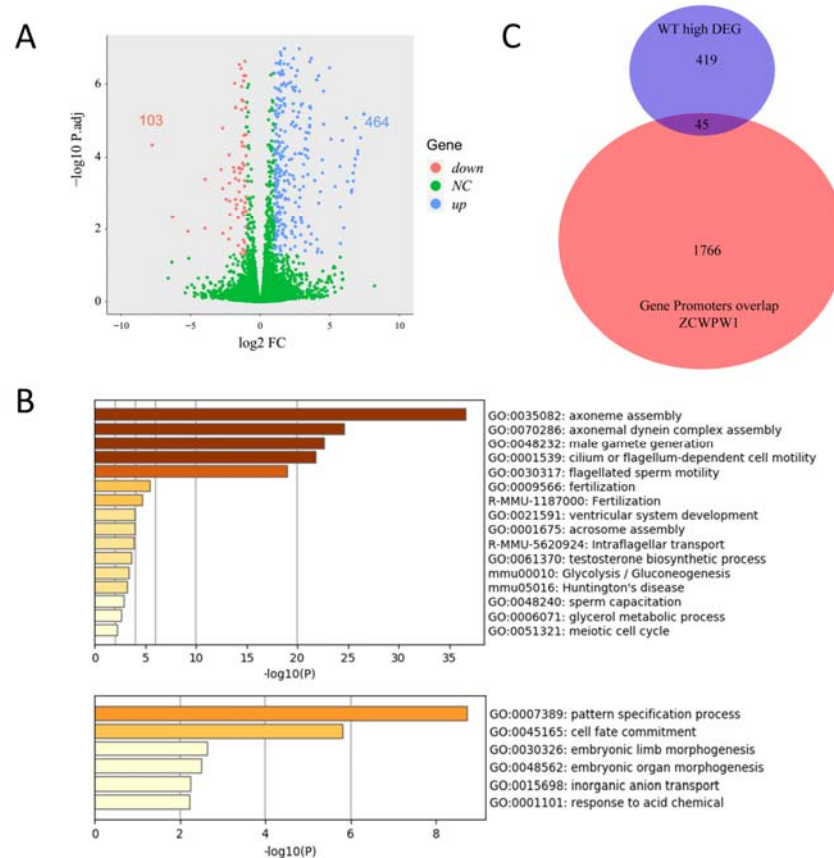
1059 Percentage of ZCWPW1 binding sites (peaks) overlapping with transposable elements (TEs)

1060 compared with the random binding sites obtained by random shuffling of the ZCWPW1 binding sites.

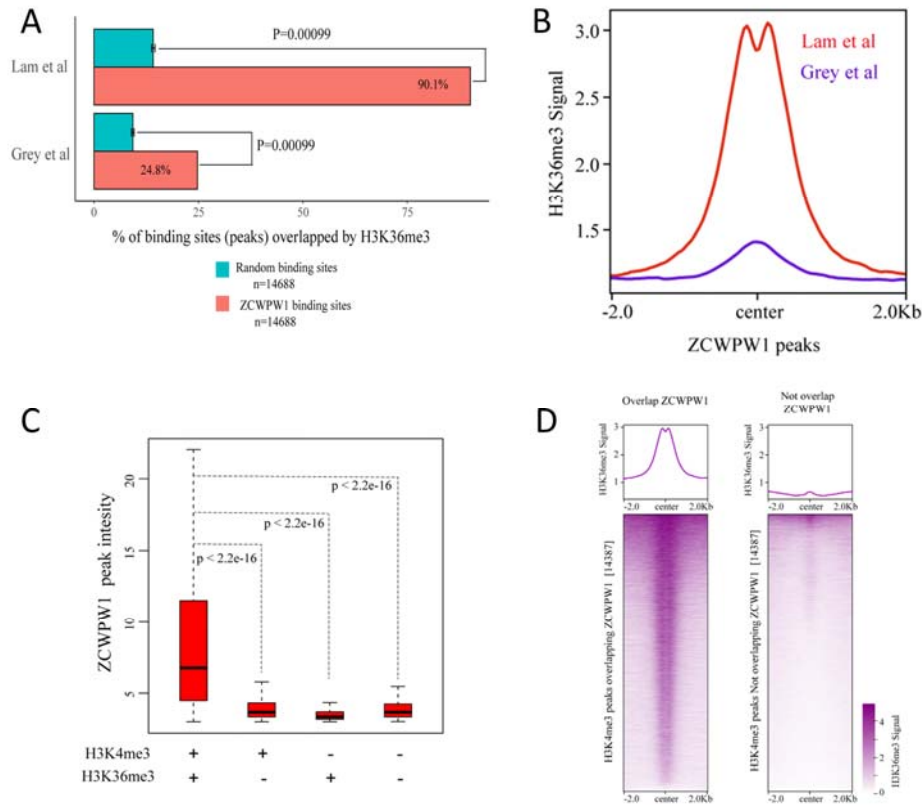
1061 The X-axis indicates the percentage of binding sites overlapping with TEs. The random groups and

1062 P-values were generated using the same method as Figure 3–figure supplement 1B. (D). Percentage of

1063 ZCWPW1 binding sites (peaks) overlapping with Alu repeats compared with the binding sites
 1064 obtained by random shuffling of the identified ZCWPW1 binding sites. The X-axis indicates the
 1065 percentage of binding sites overlapping with Alu repeats. The random groups and P-value were
 1066 generated as above.



1067
 1068 **Figure 3-figure supplement 2. Transcriptional profiling analysis of WT and *Zcwpw1*^{-/-} testes**
 1069 (A). Scatterplot of DEGs between WT and *Zcwpw1*^{-/-} at PD14. Downregulated in WT, red;
 1070 upregulated in WT, blue; no significant change (NC), green. P-adjust < 0.05 and FC ≥ 2 or FC ≤ 0.5.
 1071 (B). Functional enrichment analysis of DEGs by Metascape. The upper bar chart shows DEGs with
 1072 higher expression in WT, and the lower bar chart shows DEGs with higher expression in *Zcwpw1*^{-/-}.
 1073 (C). Venn diagram of the overlap between the genes with promoter regions overlapping ZCWPW1
 1074 binding sites and DEGs showing higher expression in WT. All RNA-seq experiments were performed
 1075 on PD14 mice with n > 3 for each genotype.

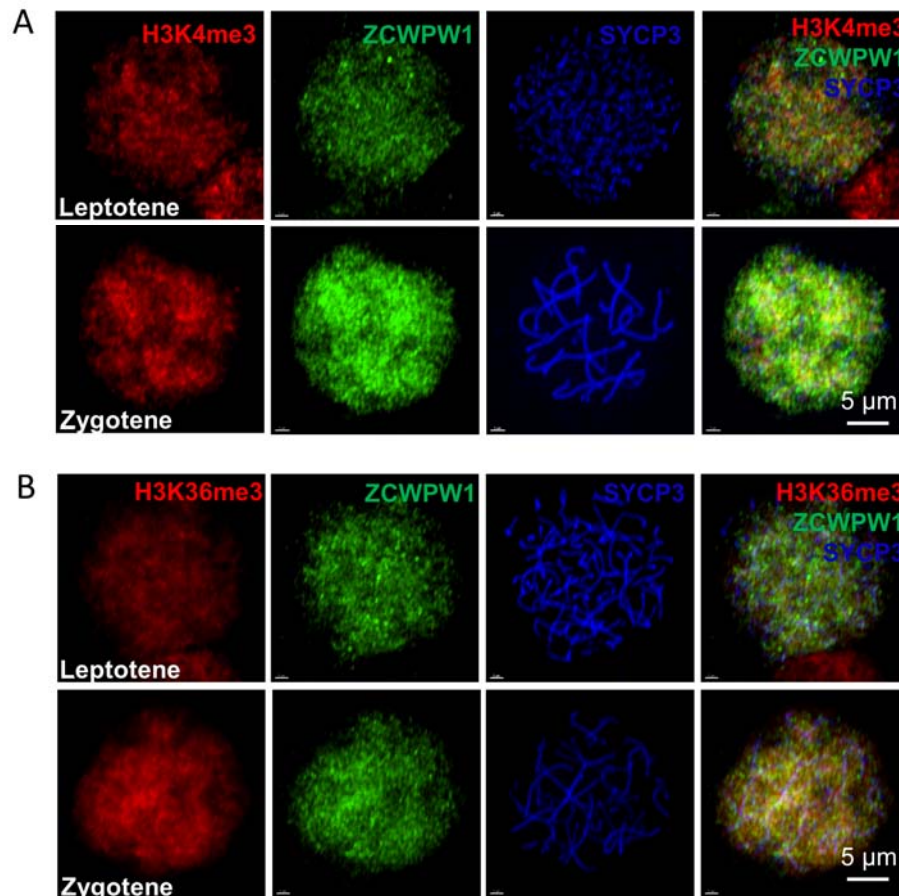


1076

1077 **Figure 3–figure supplement 3. Correlations between ZCWPW1 peaks and H3K4me3 and**
 1078 **H3K36me3 peaks**

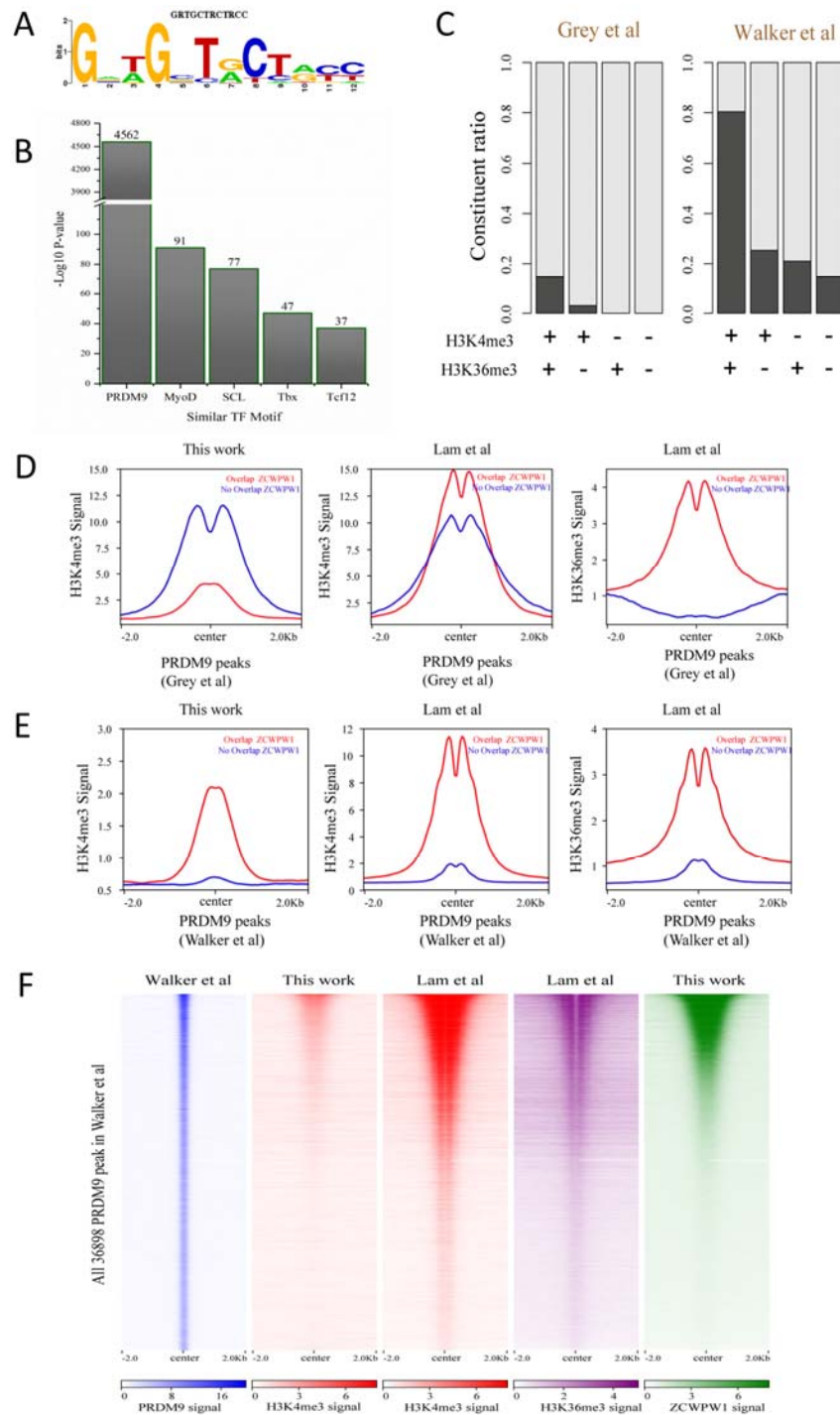
1079 (A). Percentage of ZCWPW1 binding sites (peaks) overlapping with H3K36me3 peaks identified by
 1080 Lam *et al.* (2019) or Grey *et al.* (2018), compared with the random binding sites obtained by random
 1081 shuffling of the identified ZCWPW1 peaks. The X-axis indicates the percentage of binding sites
 1082 overlapping with H3K36me3 peaks. The random groups and P-values were generated using the
 1083 method described above. (B). Profile plot of the averaged normalized H3K36me3 signal (See
 1084 Methods) obtained from Grey *et al.* (whole testes) and Lam *et al.* (isolated stage-specific
 1085 spermatocyte nuclei) in ZCWPW1 peaks. The profile shows the average values over 4-kb intervals for
 1086 all 14688 peaks (binding sites). (C). Boxplots showing the peak intensity of four ZCWPW1 groups
 1087 determined by their overlap with histone modification peaks (Lam *et al.*). + indicates overlap, -
 1088 indicates no overlap. The P-values was calculated using the two-tailed Wilcoxon rank sum test. (D).
 1089 Heatmap and averaged profile plot of the H3K36me3 signal (Grey *et al.*) on two types of H3K4me3
 1090 peaks (Grey *et al.*), including H3K4me3 peaks overlapping ZCWPW1 and H3K4me3 peaks not

1091 overlapping ZCWPW1. The 14,387 H3K4me3 peaks were randomly sampled from the total
1092 H3K4me3 peaks not overlapping with ZCWPW1 (61,384). Each row of the heatmap shows the
1093 H3K36me3 distribution on an H3K4me3 peak center \pm 2k bp. The color change from white to purple
1094 indicates a change in the normalized H3K4me3 signal from weak to strong.



1095
1096 **Figure 3–figure supplement 4. ZCWPW1, H3K4me3 and H3K36me3 localize to the nucleus in**
1097 **leptotene and zygotene spermatocytes**
1098 (A). Chromosome spreads of spermatocytes from the testes of adult WT were immunostained for
1099 H3K4me3 (red), ZCWPW1 (green), and SYCP3 (blue). Representative images of spermatocytes at
1100 leptotene and zygotene stages are shown. (B). Chromosome spreads of spermatocytes from the testes
1101 of adult WT were immunostained for H3K36me3 (red), ZCWPW1 (green), and SYCP3 (blue).
1102 Representative images of spermatocytes at leptotene (upper panels) and zygotene (lower panels)

1103 stages are shown. All experiments were performed on adult mice (6-8 weeks old) with $n > 3$ for each
 1104 genotype.

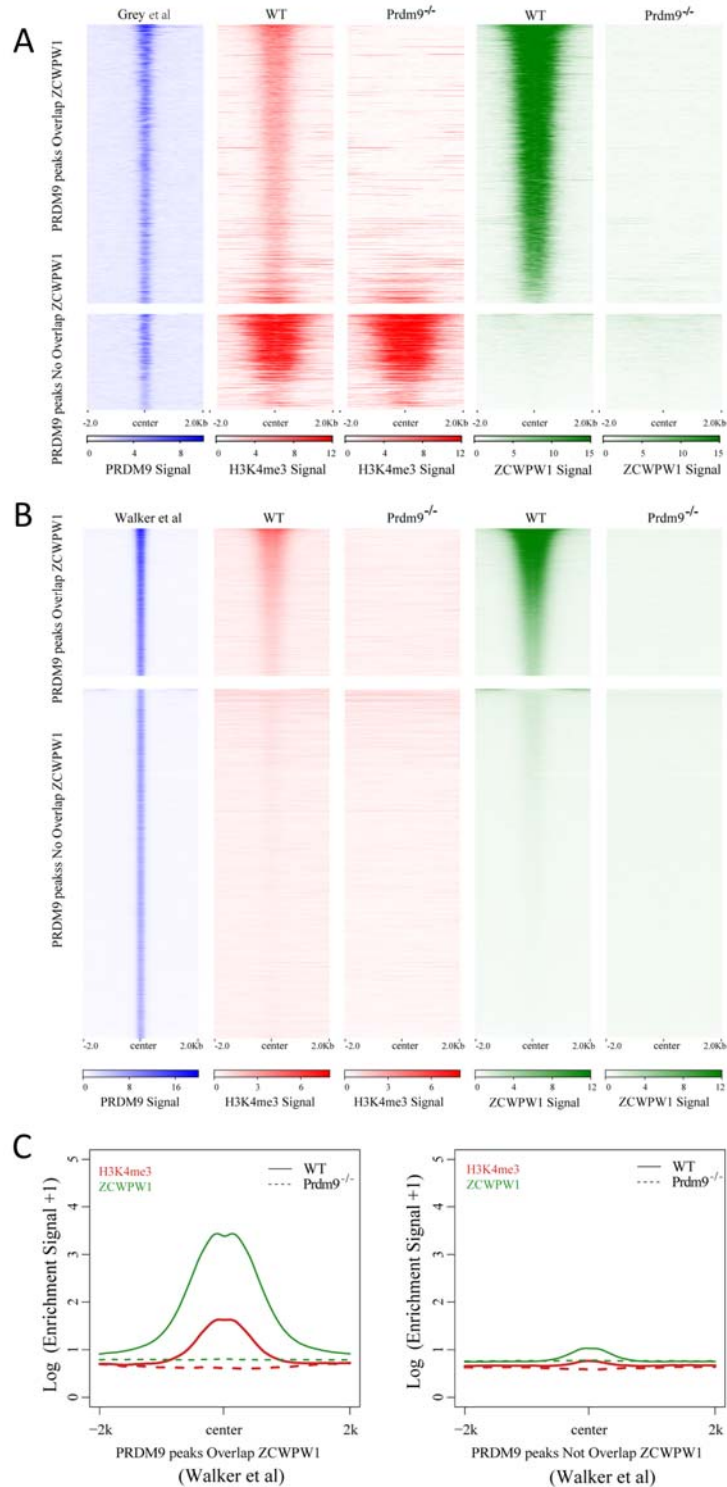


1105

1106 **Figure 4-figure supplement 1. Correlation between ZCWPW1 binding sites and PRDM9-**

1107 **induced dual histone methylation**

1108 (A). The rank-first *de novo* binding motif of ZCWPW1. (B). The similarity of this ZCWPW1 binding
1109 motif with those of other transcription factors. (C). Barplots showing the constituent ratio of four
1110 groups of ZCWPW1 peaks according to their overlap with PRDM9-induced marks. Black indicates
1111 overlap, white indicates no overlap. The four ZCWPW1 groups classified by their overlap with
1112 histone modification peaks (Lam *et al.*). + indicates overlap, - indicates no overlap. (D). Profile plot
1113 of averaged H3K4me3 and H3K36me3 signals in different types of PRDM9 peaks generated by Grey
1114 *et al.* The profile shows the average values over 4-kb intervals for all 2,601 detected PRDM9 binding
1115 sites. (E). Profile plot of averaged H3K4me3 and H3K36me3 in different types of PRDM9 peaks
1116 generated by Walker *et al.*; the profile shows the average values over 4-kb intervals for all 36898 of
1117 the detected PRDM9 binding regions. (F). Heatmap showing the correlation among H3K4me3,
1118 H3K36me3, and ZCWPW1 in the PRDM9 peaks (Walker *et al.*). Each row in the heatmap represents
1119 a PRDM9 binding site of ± 2 kb around the center and ranked from the highest to the lowest according
1120 to ZCWPW1 signal intensity. Color indicates normalized ChIP-seq signal (see methods).

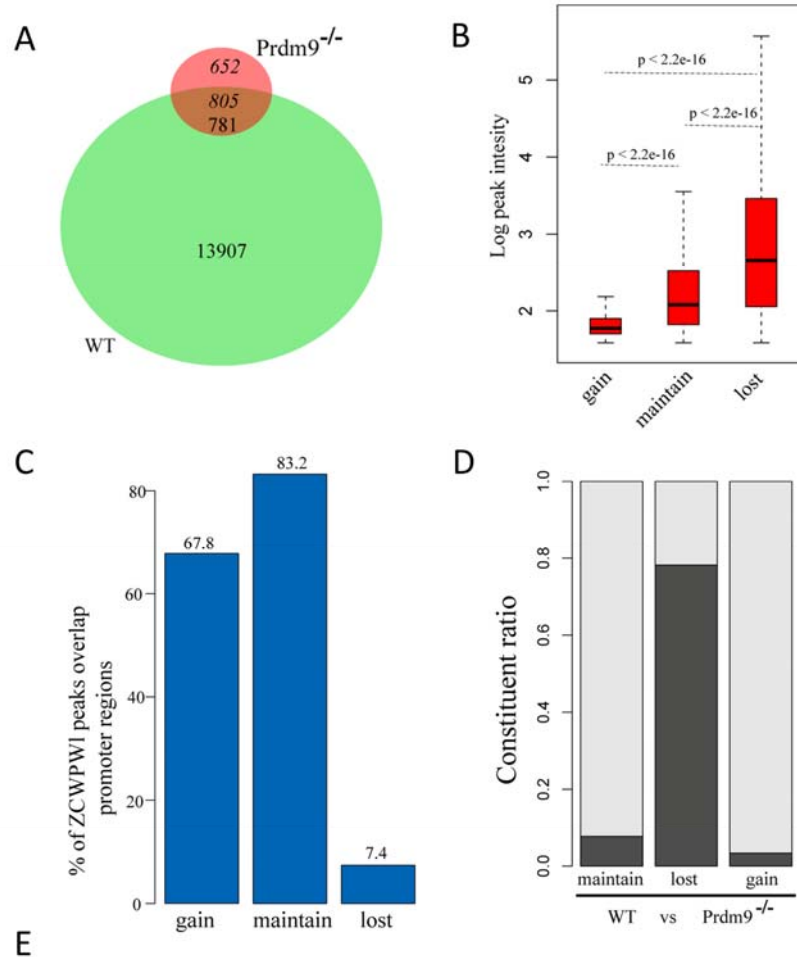


1121

1122 **Figure 4-figure supplement 2. Correlation between ZCWPW1 chromatin occupancy and**

1123 **PRDM9-induced H3K4me3**

1124 (A). Heatmap showing H3K4me3 and ZCWPW1 signals obtained in this work, in two types of
1125 PRDM9 peaks (Grey *et al.*) following *Prdm9* knockout. Each row in the heatmaps represents a
1126 PRDM9 binding site of ± 2 kb around the center and ranked from the highest to the lowest according
1127 to PRDM9 density. Color indicates ChIP-seq density. (B). Heatmap showing H3K4me3 and
1128 ZCWPW1 signals obtained from this work, on two types of PRDM9 peaks identified by Walker *et al.*
1129 following *Prdm9* knockout. Each row in the heatmaps represents a PRDM9 binding site of ± 2 kb
1130 around the center and ranked from the highest to the lowest according to PRDM9 density. Color
1131 indicates ChIP-seq density. (C). Profile plot of averaged H3K4me3 and ZCWPW1 signals obtained in
1132 this work and in two types of PRDM9 peaks identified by Walker *et al.* following *Prdm9* knockout.
1133 The Y-axis indicates the log base-2 transformation of the normalized signals. All ChIP-seq
1134 experiments were performed using PD14 mice with $n > 3$ for each genotype.



3028 ZCWPW1 peaks: Lost but not overlap with PRDM9

	Name	P-value	Target Sequences with Motif	Background Sequences with Motif
	PRDM9	1e-606	994(32.6%)	117(3.88%)

1135

1136 **Figure 4–figure supplement 3. Change in ZCWPW1 chromatin occupancy following *Prdm9***

1137 **knockout**

1138 (A). Venn diagram showing the overlap of the ZCWPW1 peaks between WT and *Prdm9* knockout

1139 (*Prdm9*^{-/-}). ZCWPW1 peaks were grouped by their detection in either WT, *Prdm9*^{-/-}, or both as

1140 either gained (652) – indicating peaks only found after *Prdm9* knockout, maintained (781) –

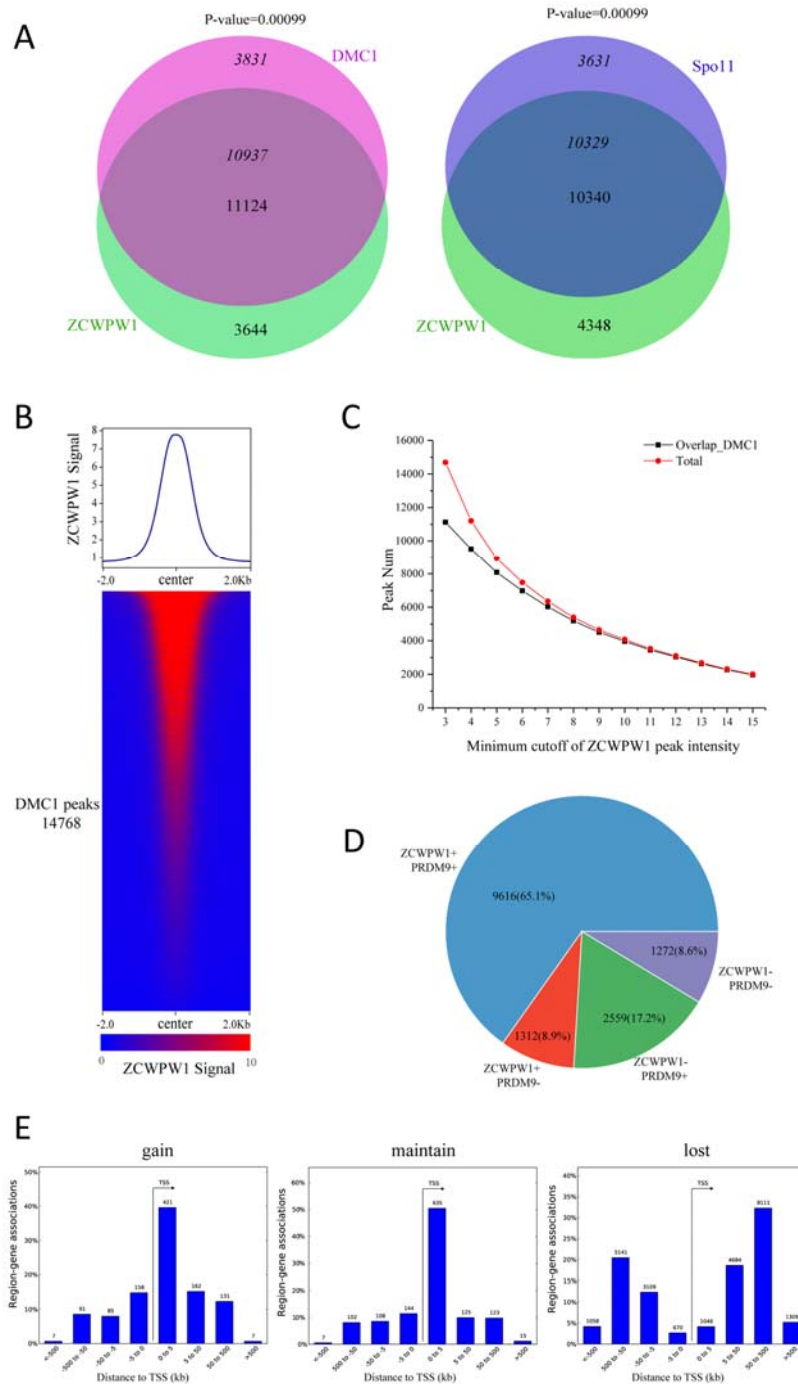
1141 indicating peaks found in both backgrounds, or lost (13,907) – indicating peaks found only in WT.

1142 (B). Boxplots showing the peak intensity of the three ZCWPW1 groups. The Y-axis indicates the log

1143 base-2 transformation of normalized signals. P-values were calculated by two-tailed Wilcoxon rank

1144 sum test. (C). Barplots showing the percentage of ZCWPW1 peaks overlapping with promoter

1145 regions for the three groups of ZCWPW1 peaks. **(D)**. Barplots showing the constituent ratio of each
1146 ZCWPW1 peak group according to whether they overlapped with PRDM9, which includes the
1147 merged peaks of Grey *et al* and Walker *et al*. Black indicates overlap, white indicates no overlap. **(E)**.
1148 Motif analysis of the lost ZCWPW1 peaks that did not overlap with merged PRDM9 peaks. The value
1149 of background had been transformed to the condition that the ratio was stable and the number of
1150 regions was scaled to 3028.



1151

1152 **Figure 5–figure supplement 1. Correlation between the chromatin occupancy of ZCWPW1 and**
 1153 **DMC1**

1154 (A). Venn diagram showing the overlap of the DMC1 (Grey *et al*) and Spo11 (Lange *et al.*) peaks with
 1155 ZCWPW1 binding sites. P-values were calculated using the permTest (see Methods, ntimes=1000).

1156 **(B).** Heatmap and profile plot of the ZCWPW1 signal in all DMC1 peaks. Each row in the heatmap
1157 represents a DMC1 binding site of ± 2 kb around the center and ranked according to ZCWPW1 signal
1158 from the highest to the lowest. Color indicates the normalized ChIP-seq signal (See methods). **(C).**
1159 Line plots showing the overlap of ZCWPW1 peaks with DMC1 peaks based on different minimum
1160 cutoff values for ZCWPW1 peak intensity. The Y-axis indicates the overlap number, and the X-axis
1161 indicates the minimum cutoff of ZCWPW1 peak intensity. The red line represents the total number of
1162 ZCWPW1 peaks with a specific minimum cutoff for ZCWPW1 peak intensity. The black line
1163 represents the overlap number of ZCWPW1 peaks with DMC1 peaks with a specific minimum cutoff
1164 for ZCWPW1 peak intensity. **(D).** Pie chart showing the ratio of four DMC1 peak groups (Grey *et al.*)
1165 determined by their overlap with merged PRDM9 peaks (Grey *et al.*; Walker *et al.*) and ZCWPW1
1166 peaks. + indicates overlap, - indicates no overlap. **(E).** The number of region (peak)-gene associations
1167 among distance stratifications of ZCWPW1 peaks in three subtypes within the TSS ± 1000 kb region.

1168

1169 **Supplemental File 1. Summary of all ChIP-seq experiments indicating antibodies, samples,**
1170 **replicates, genotype and data source.**

1171

1172 **Supplemental File 2. ZCWPW1 peaks in WT and *Prdm9* knockout mice**

1173

1174 **Figure 1-source data 1. Number of DMC1 and RAD51 foci in Figure 1D and 1F**

1175

1176 **Figure 1 figure supplemental 2-source data 1. Number of synapsed chromosome pairs per cell**
1177 **in Figure 1 figure supplemental 2C**

1178

1179 **Figure 1 figure supplemental 3-source data 1. Number of MSH4 and RNF212 foci in Figure 1**
1180 **figure supplemental 3B and 3D**

1181